Evolution of Au(111) electrode surface in different electrolytes and conditions studied with a home-made EC-STM

Behjati, S.

Appendix A

Supporting information for chapter 2

A.1 Introduction

As explained in the introduction of this thesis, EC-STM is one of the instruments that can help chemists to have a closer look at the surface of electrodes. Many improvements have been made[111, 112] since the first successful experiments of atomic resolution in aqueous electrolytes[113]. However, there are always some limitations in these instruments that prevent us from recording valid data in certain measurements. For instance, the electrolyte inside the cell is not renewed with fresh electrolyte. This can be problematic for long measurements of e.g. the hydrogen evolution reaction (HER) or the oxygen evolution reaction (OER). The concentrations of species can alter in the electrolyte, and impurities can accumulate on the electrode surface, which is not desirable. One way to tackle this is to have a flow of electrolytes inside the cell. Thus, a pumping system is required to pump the fresh electrolyte into the cell and pump out the used electrolyte. Because of the small volume of the EC-STM cell, it is essential to have precise control over the flow rates at the inlet and outlet. The errors in pumping rates can result in overflow or underflow conditions. Moreover, the surface tension plays a significant role because of the small size of the cell. At this dimension, the dominant force is not gravity anymore, and we must take surface tension into consideration. Finally, the flow can make some minor pressure differences across the tip and exert some lateral forces toward the tip during the image recording,

which can turn into a reason for extra drifts. The electrolyte flow near the sample surface is crucial because it can affect the electrochemical reactions on the surface. A proper flow near the sample surface is required, and the best way to study this characteristic is computational fluid dynamics (CFD). CFD is a numerical method for the simulation of fluid flow in a system. The Residence Time Distribution (RTD) in a reactor can also be calculated by this method. The RTD is an efficient tool to study the flow pattern like flow mixing behavior in chemical reactors[114]. In a nutshell, the time that different fluid elements spend in a continuous process unit (or steady-state continuous flow reactor) is called residence time distribution (RTD) of the fluid elements in that process unit (reactor). The RTD in a reactor is determined experimentally by injection of an inert tracer into the stream flowing through the reactor at time $t = 0$ in the reactor inlet and then measuring the concentration of the tracer over time in the reactor outlet. The response concentration curve, known as the RTD function, provides useful information about the process stream dynamics[115]. A critical consideration in the system's design is the prevention of vortex formation within the cell, as this phenomenon can drastically alter the average residence time distribution, thereby impairing overall performance. To address this issue, an extensive study was undertaken to evaluate the effects of cell geometry and dimensions. In addition, the influence of operational parameters, such as the pumping rate and the electrolyte height, was investigated. The results of these analyses will be presented and discussed in the following sections.

A.2 Numerical Model (FLOW-3D)

Simulation of flow in the cell was performed by FLOW-3D Software[116] within a two-phase system (water-air) in a three-dimensional numerical model. In FLOW-3D, all equations are formulated with area and volume porosity functions. This method is called FAVOR or Fractional Area/Volume Obstacle Representation Method[116]. In the FAVOR method, the meshes are rectangular, and boundaries are located in the mesh domain by using a porosity technique in which the volume fraction (V_F) is zero within obstacles and unity where the cell is fully filled with fluid. For $0 < V_F < 1$, the cell is partially occupied by the obstacle (e.g., near the surface). By this technique, many numerical problems in a simulation, such as instability and algorithm complication can be eliminated. FLOW-3D solves the Reynolds averaged Navier-Stokes equations (continuity and momentum in the three directions) as shown in equations A.1-A.4, respectively[116]. V_F is the cell fractional volume; ρ is the fluid density; u, v,

and w are velocity components in the x, y, and z directions; A_x, A_y, and A_z are the cross-sectional area of the flow in x, y, and z directions; p is pressure; G_x, G_y, and G_z are gravitational components in three directions; and F_x, F_y, and F_z are viscous accelerations in three directions.

$$V_F \frac{\partial \rho}{\partial t} + \frac{\partial (uA_x)}{\partial x} + \frac{\partial (vA_y)}{\partial y} + \frac{\partial (wA_z)}{\partial z} = 0 \tag{A.1}$$

$$\frac{\partial u}{\partial t} + \frac{1}{V_F}\left[uA_x \frac{\partial u}{\partial x} + vA_y \frac{\partial u}{\partial y} + wA_z \frac{\partial u}{\partial z}\right] = -\frac{1}{\rho}\frac{\partial p}{\partial x} + G_x + F_x \tag{A.2}$$

$$\frac{\partial v}{\partial t} + \frac{1}{V_F}\left[uA_x \frac{\partial u}{\partial x} + vA_y \frac{\partial u}{\partial y} + wA_z \frac{\partial u}{\partial z}\right] = -\frac{1}{\rho}\frac{\partial p}{\partial y} + G_y + F_y \tag{A.3}$$

$$\frac{\partial w}{\partial t} + \frac{1}{V_F}\left[uA_x \frac{\partial u}{\partial x} + vA_y \frac{\partial u}{\partial y} + wA_z \frac{\partial u}{\partial z}\right] = -\frac{1}{\rho}\frac{\partial p}{\partial z} + G_z + F_z \tag{A.4}$$

In FLOW-3D Software, the VOF method is used for free surface tracking. That is a simple and efficient method for modeling free surface profiles in two-dimensional and three-dimensional meshes and is based on the work of Nichols and Hirt[117]. This method is an extended formulation of a previous method named Marker and Cell (MAC) method. In the MAC method, a number of marker particles are defined that moves in the computational domain, so the grids that contain markers are occupied by fluid, and those without markers are empty and free surface is located in grids that contain marker particles and at the same time have at least one neighboring grid cell that is empty[118]. MAC is a computationally expensive method compared to VOF because the new method does not need to define particles, and occupancy of the cells in the grid is parameterized using a function named F. F is a function that has a value of unity in regions occupied by fluid and zero in regions containing no fluid. So for F between 0 and 1, cells contain a free surface. The VOF formulation in the form of FAVOR is given as equation A.5.

$$\frac{\partial F}{\partial t} + \frac{1}{V_F}\left[\frac{\partial}{\partial x}(FA_x u) + \frac{\partial}{\partial y}(FA_y v) + \frac{\partial}{\partial z}(FA_z w)\right] = 0 \tag{A.5}$$

To investigate the residence time distribution (RTD) of the cell, two distinct approaches can be employed: particle tracking and the Local Mean Age (LMA) of the fluid. In the particle tracking approach, the RTD is determined by simulating the injection of particles at the reactor's inlet and measuring their concentration at the outlet. This method is called "pulse experiment" and the experimental process for

this is described by Levenspiel (1999)[119]. In CFD, a convection-diffusion equation is employed to track the motion of a finite number of marker particles injected at the inlet boundary of the computational domain[]. These marker particles are massless and significantly smaller than the mesh size within the domain. They do not influence the fluid dynamics but instead move with the mean flow while also undergoing diffusion, governed by a specified diffusion coefficient. From the resulting concentration curve ($C(t)$), which is the particle concentration at a certain location as a function of time, the normalized concentration ($E(t)$) can be calculated by equation A.6. The mean residence time (τ) is then defined as equation A.7. The dimensionless variance (σ) in equation A.8 is a metric used to quantify the spread or dispersion of residence times in a system relative to the mean residence time. A low value of the dimensionless variance typically indicates a plug flow behavior with minimal dispersion whereas a high value suggests significant dispersion, often associated with mixing or deviations from ideal plug flow.

$$E(t) = \frac{C(t)}{\int_0^\infty C(t)\,dt} \tag{A.6}$$

$$\tau = \int_0^\infty tE(t)\,dt \tag{A.7}$$

$$\sigma^2 = \frac{\int_0^\infty (t-\tau)^2 C(t)\,dt}{\int_0^\infty C(t)\,dt} \tag{A.8}$$

In the second approach which named local mean age (LMA), the average age of the fluid throughout the entire cell can be calculated. This represents the average time taken by fluid particles to travel from an inlet (or a reference point) to a specific location in the domain. The resulting distribution of the local average fluid age is visualized as iso-contours within the spatial domain.

A.2.1 Geometry and Mesh

The geometry under CFD study consists of three key components in the region of interest: counter electrode, cell, and scanning tip. These components influence the flow patterns within the domain and subsequently affect the conditions for electrochemical reactions. The components, as shown in Figure A.1, are described below:

The Cell serves as the main container into which fresh solution is pumped through a 0.6 mm diameter inlet located on the left-hand side wall. The stale solution exits

through a 0.6 mm diameter outlet on the right-hand side wall at the same height as the inlet. At the bottom of the cell, a 3 mm diameter hole accommodates the sample, mounted underneath the cell. To prevent leakage, an O-ring, 1 mm thick, is placed between the sample and the cell. The most critical area of the cell is the bottom of this hole, where the electrochemical reactions occur.

The Counter electrode consists of a long, inert wire, typically made of platinum or gold. Since the wire is immersed in the solution, it can influence the flow within the cell. Therefore, the shape and placement of the electrode are critical. As shown in Figure A.1, the counter electrode is positioned near the edge of the wall at the bottom of the cell.

The Scanning tip is responsible for scanning the surface of the sample at the bottom of the cell and recording geometrical data with atomic resolution. The tip is a conductive wire oriented perpendicularly to the sample surface. Its effect on the flow pattern is significant and cannot be ignored. The tip is surrounded by an insulating layer to prevent unwanted electrochemical reactions along its length. Only the metal apex of the tip is exposed to the solution to record the tunneling current. However, the exposed area is negligible compared to the mesh size, and its impact on the overall flow pattern is minimal.

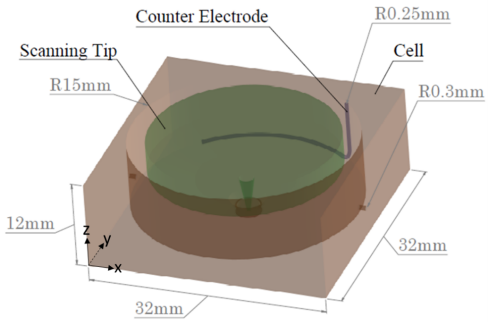

Figure A.1: Circular cell geometry showing the dimensions and the different components.

The system for CFD simulations consists of two primary regions: the flow domain and the solid domain. As previously mentioned, the flow domain is divided using rectangular meshes. This type of mesh is straightforward to generate and contributes to the stability of the numerical solution. The mesh size was selected to be less than 0.2 mm, which provides an appropriate balance between achieving a reasonable number of nodes and maintaining a manageable simulation runtime.

A.2.2 Boundary conditions

In this study, a two-phase flow was considered, with water as the first phase and air as the second. The flow was modeled under the assumptions of an isothermal, incompressible, Newtonian fluid with constant density and viscosity. The density and viscosity of water at room temperature were assumed to be 998 $kg.m^{-3}$ and 1 $g.m^{-1}.s^{-1}$, respectively. The ambient air pressure was set to 1.013×10^5 Pa. Constant velocity boundary conditions were applied at the inlet and outlet of the cell, while no-slip conditions were enforced at all solid walls. The Reynolds number was calculated to be 54 in the inlet/outlet pipe and lower throughout the cell, indicating laminar flow. The effects of surface tension and gravity were also considered. Gravity can be neglected in the simulation if the dimension of the cell is smaller than the capillary length of water ($l_{\text{cap}} \approx 2.7\,\text{mm}$)[120]. The surface tension of water at room temperature was considered constant at 0.072 $N.m^{-1}$. The effects of wall adhesion were included, with contact angles of 80° for the cell, 115° for the scanning tip, and 40° for the counter electrode.

The simulation was conducted with a time-step ranging from 1 to 10 μs. The governing equations were solved until the velocity field reached a steady-state condition. The dye tracer was introduced at the cell inlet from $t = 0\,\text{s}$ to $t = 2\,\text{s}$. For $t > 2\,\text{s}$, the tracer concentration at the inlet was set to zero. Simultaneously, the tracer concentration was detected at the outlet. Two flux planes were defined perpendicular to the inlet and outlet. The tracer concentration values were extracted from the simulation outputs corresponding to these planes.

Boundary conditions were applied as follows:

- X_{min} and X_{max} : Constant velocity at the inlet and outlet.
- Z_{max}: Constant pressure.
- Y_{min}, Y_{max}, and Z_{min}: Wall boundary conditions, as these planes correspond to solid materials.

A non-zero initial fluid height was considered to reduce the total runtime. To avoid any confusion, the initial height is defined the distance between the sample surface and fluid height.

A.3 Results and discussion

In addition to the main circular cell (Figure A.1), the Rhombic Cell (Figure A.2a) was designed to minimize undesirable hydraulic flow patterns, such as back mixing and dead volume, thereby improving the overall mean residence time distribution (RTD) within the cell and near the sample surface. The Rhombic Cell with Groove (Figure A.2b) retains the general shape of the simple Rhombic Cell but includes a groove at its base to improve the performance further.

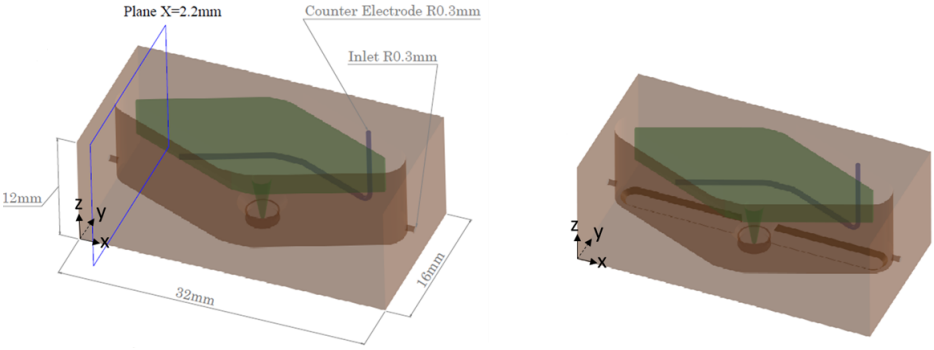

(a) **(b)**

Figure A.2: a) rhombic cell, b) rhombic cell with groove

The results of the normalized concentration for the initial water height of 1mm with three different inlet velocities (3, 6, and 9 cm/s) for the circular cell are presented in Figure A.3. It is evident that the higher velocity helps the tracers to reach the detector at the output sooner and it shifts the highest concentration peak to lower time.

Figure A.4 presents the LMA contours in the midplane (y = 0) for three different velocities. Similarly, Figure A.5 illustrates the LMA contours for a plane parallel to and close to the sample surface in the circular cell, with an initial water height of 1 mm and varying inlet velocities. These contours demonstrate the impact of higher velocities on RTD.

Similar simulations were done for the rhombic cell and Figure A.6 presents the normalized concentration function for different initial water heights and inlet velocities. As previously discussed, higher velocities result in improved performance, which is also evident for the Rhombic Cell. A comparison at a fixed velocity (3 $cm.s^{-1}$) across all initial electrolyte heights in Figure A.6 indicates that lower electrolyte heights lead to better RTD performance.

Figure A.7 presents the LMA results for a plane parallel to and near the sample

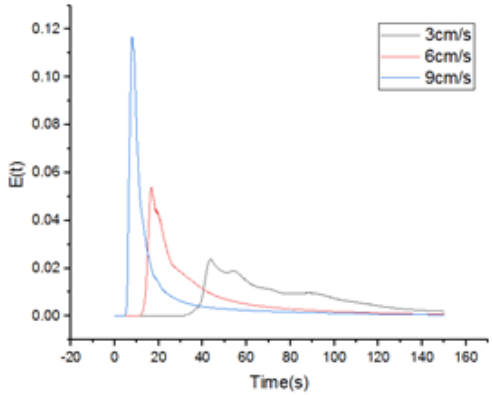

Figure A.3: $E(t)$ function for 1 mm initial fluid height in the Circular Cell for three different inlet velocities

surface in the Rhombic Cell, with an initial water height of 1 mm and varying inlet velocities. A significant improvement is observed compared to the Circular Cell (Figure A.5).

The final version of the cell design is the Rhombic Cell with a groove at its bottom. Figure A.8 presents the $E(t)$ function results for various initial electrolyte levels and inlet velocities for this model, while Figure A.9 displays the LMA contours.

When fluid flows through an ideal reactor, one of two primary assumptions is typically used to facilitate performance analysis. The first assumption is that the fluid in the reactor is thoroughly mixed, resulting in uniform properties throughout the reactor volume. This scenario applies to stirred reactors or blending systems. The second assumption, referred to as "plug flow," suggests that all fluid elements enter the reactor simultaneously, travel through it at the same velocity along parallel paths, and exit at the same time. This assumption is particularly valid in cases such as laminar flow within pipes[121]. Thus, ideal reactors exhibit two primary flow patterns: plug flow and mixed flow. These patterns result in distinctly different behaviors, and reactor design often aims to approach one of these idealized flow regimes. However, real reactors deviate from these ideal patterns due to phenomena such as fluid channeling, recycling, or the presence of stagnant or dead zones within the reactor. Such flow irregularities should be minimized, as they reduce reactor performance[119]. Various models have been developed to predict reactor behavior under real conditions, capturing flows that may align more closely with plug flow, mixed flow, or intermediate patterns. By comparing experimental residence time distribution (RTD) curves to theoretical models, the most suitable model for a given reactor can often be identified. Although the fit

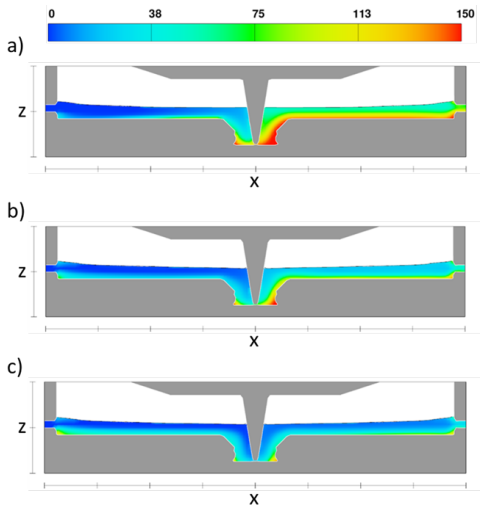

Figure A.4: LMA contour of circular cell in the midplane (y=0) at velocities of a) 3, b) 6, and c) 9 $cm.s^{-1}$.

may not be perfect, these models provide a reasonable approximation of the actual $E(t)$ curve[119]. In summary, these models are valuable tools for understanding flow behavior and diagnosing inadequacies in real reactors[119].

In compartment models, the reactor volume is divided into three distinct regions: the plug flow region, the mixed flow region (together referred to as the active volume), and the dead or stagnant region[119]. The $E(t)$ function for a complete plug flow in a reactor resembles a pulse function, where all injected elements have the same residence time within the reactor. Under real conditions, when the $E(t)$ function shows a sharp peak with a short tail, the flow can be approximated as a plug flow. In contrast, for a complete mixing flow, the $E(t)$ function follows a decaying exponential curve over time. However, in real reactors, flow behavior is typically a combination of plug flow and mixing flow, resulting in an $E(t)$ function that includes a sharp peak followed by a tail[119].

A comparison of the circular cell (Figure A.3) with the rhombic cell (Figure A.6b) demonstrates that the rhombic cell exhibits behavior closer to plug flow, representing an ideal reactor, and performs better than the circular cell. In all three models, increasing the inlet velocity while maintaining a constant initial electrolyte height (1 mm) results in higher $E(t)$ peaks with shorter tails. This indicates that as inlet velocity increases, injected particles exit the cell more rapidly, with more uniform

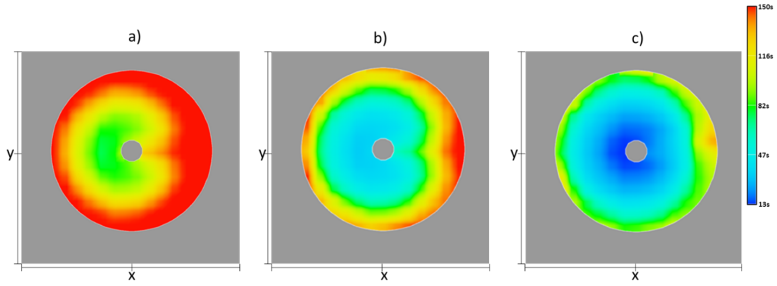

Figure A.5: LMA contour of the circular cell parallel and near the sample surface at velocities of a) 3, b) 6, and c) 9 $cm.s^{-1}$.

flow and reduced dispersion. Consequently, at higher velocities, the cell behaves more similarly to an ideal plug flow reactor. The dependency of outlet tracer concentration on the initial electrolyte height, for a constant velocity of 6 $cm.s^{-1}$, is illustrated in Figures A.10a and A.10b for the rhombic cell and the rhombic cell with a groove, respectively. A similar trend to that observed with increasing inlet velocity at a constant height is seen when reducing the initial electrolyte height at a constant inlet velocity. Specifically, as the initial height decreases, the $E(t)$ curves become narrower and exhibit shorter tails, confirming that the reactor flow approaches ideal plug flow conditions under these circumstances.

While RTD calculations can predict the presence of dead zones within the cell, LMA (Local Mean Age) provides additional insight by identifying their precise location and dimensions. In essence, LMA calculates the average time required for a fluid element to travel from the inlet to a specific point within the cell domain.

Figures A.5, A.7, and A.9 illustrate the distribution of local fluid age on a plane parallel to and close to the sample surface (0.2 mm) for the circular, rhombic, and rhombic with groove designs, respectively. In all three models, the highest fluid ages occur in the stagnant zones near the O-ring. Furthermore, in all designs, increasing the inlet velocity reduces the size and extent of dead zones. For a more quantitative comparison, the average LMA values for each design at different inlet velocities are plotted in Figure A.11. The rhombic cell performs better at lower velocities, while the rhombic cell with a groove outperforms at higher velocities. This improvement at higher speeds is likely due to the formation of a direct flow path from the inlet to the sample surface in the grooved design. The ultimate objective is to achieve optimal LMA near the sample surface with minimal pumping speed. Higher pumping speeds introduce additional forces on the scanning tip, which can cause operational

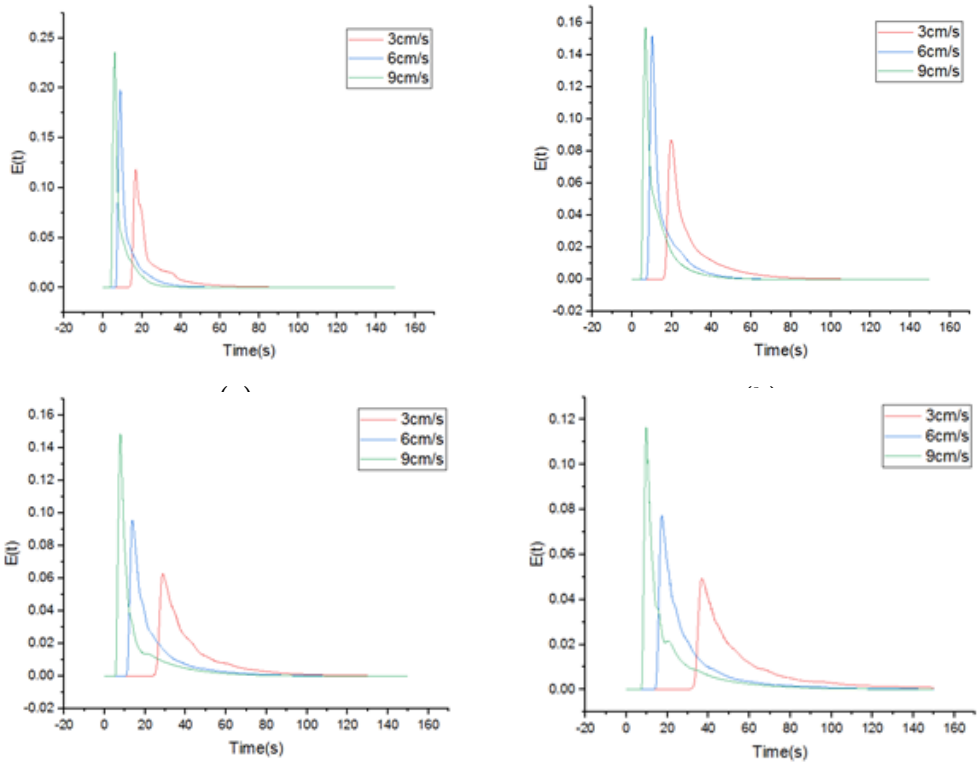

Figure A.6: $E(t)$ function result for rhombic cell design at three velocities for different initial electrolyte levels, a) 0.7, b) 1, c) 1.5, and d) 2 mm.

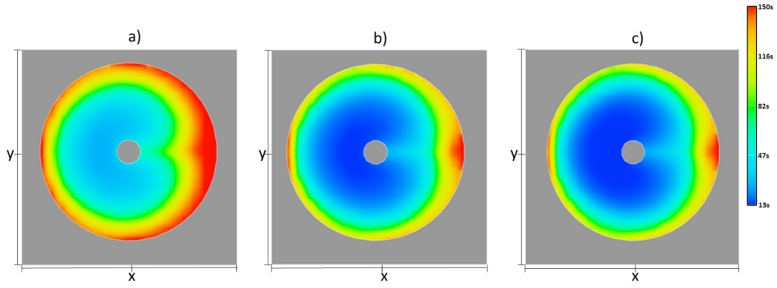

Figure A.7: LMA contour of rhombic cell parallel and near the sample surface at velocities of a) 3, b) 6, and c) 9 $cm.s^{-1}$.

challenges.

The effects of initial conditions and cell type on flow behavior were analyzed based on the residence time distribution (RTD) and LMA near the sample surface. Results indicate that the rhombic cell is highly suitable as a flow medium, particularly at low inlet velocities, as evidenced by its sharper E(t) curve peaks and shorter tails compared to the circular cell. This reflects reduced axial dispersion and a flow closer to a plug flow. At high velocities, the rhombic cell with grooves performed better than the plain rhombic cell. However, at low velocities, the LMA near the sample surface was lower in the rhombic cell. Consequently, the rhombic cell was identified as the optimal design for the EC-STM system.

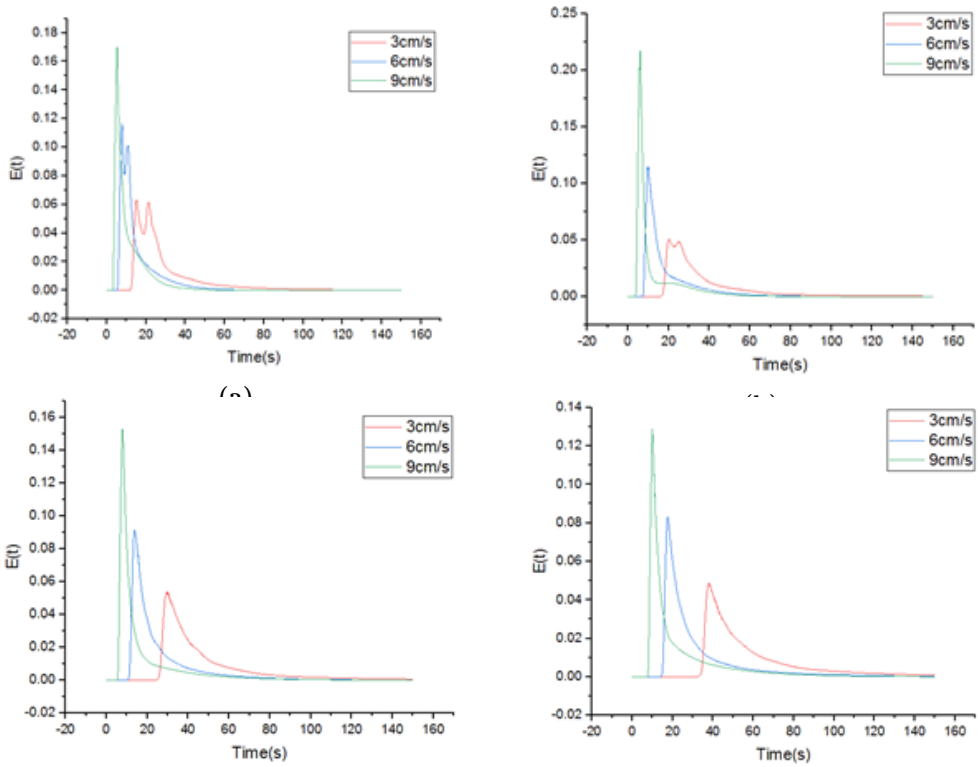

Figure A.8: $E(t)$ function result for rhombic cell with a groove at three velocities for different initial electrolyte levels, a) 0.7, b) 1, c) 1.5, and d) 2 mm.

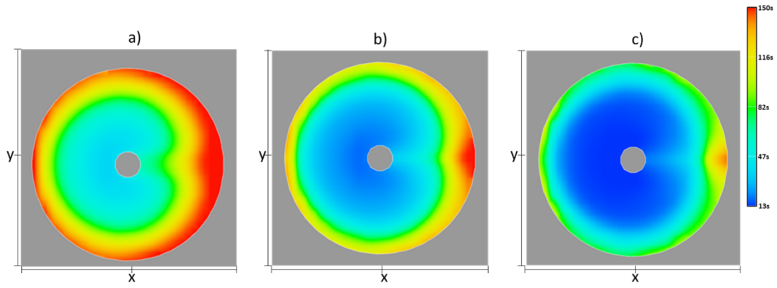

Figure A.9: LMA contour of rhombic cell with a groove, parallel and near the sample surface at velocities of a) 3, b) 6, and c) 9 $cm.s^{-1}$.

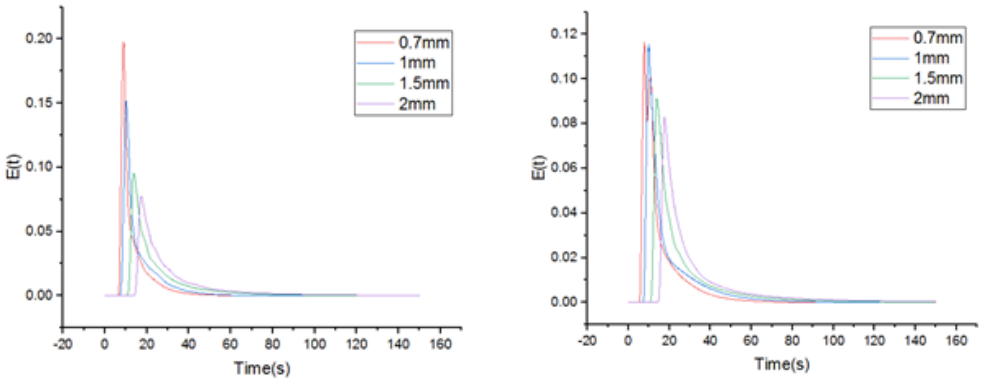

Figure A.10: $E(t)$ function for different initial heights with the inlet velocity of 6 $cm.s^{-1}$ for a) rhombic cell, b) rhombic cell with groove.

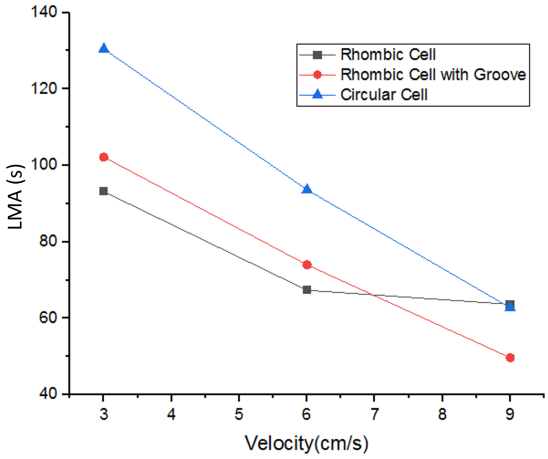

(a)

Figure A.11: Average LMA value at the plane near the sample surface for all designs with initial electrolyte height of 1 mm at different speeds.

Appendix B

Supporting information for chapter 3

B.1 Lifting the reconstruction for the experiment with holding the potential

The EC-STM image in Figure B.1a was initially recorded at 0 V just after the thermal annealing. The stripe reconstruction is visible, indicating that the sample is in good condition to start the experiment. There is a screw dislocation at the bottom-left part of the image which is a result of a defect in the crystal[122]. Subsequently, a voltage sweep from 0 to 0.2 V was applied, and Figure B.1b was recorded at 0.2 V. The image shows some defects/islands forming almost at the center of the imaged region. At this potential, we do not expect the lifting of the reconstruction since the electrode potential is lower than the potential of zero charge. It is possible to see the stripe reconstruction near the formed island which proves that the island formation cannot be due to the lifting of the reconstruction. After the potential was swept from 0.2 to 0.4 V, Figure B.1c was recorded at 0.4 V, depicting the two islands as a defect at the center. After sweeping the potential to 0.6 V, Figure B.1d was recorded, showing the generation of the small islands in the defect area. With a further sweep to 0.7 V, Figure B.1e was recorded, indicating some major changes in the step lines. It can be seen that the reconstruction lines are not as impacted as the pristine surface and they are not entirely parallel anymore. At 0.8 V, Figure B.1f was recorded, and lifting the reconstruction led to the formation of small islands all over the terraces. At 0.88 V

and 0.98 V, Figure B.1g and B.1h were recorded, respectively. By comparing Figure B.1f and B.1h, one can conclude that the island size increased at the expense of the smaller islands on the large terraces.

B.2 HHCF result for the instant frames

Figure B.2a shows the HHCF for the instant frames in the experiment with holding potential in the double layer. As expected, increasing the cycle number increases the roughness magnitude and the correlation length shifts toward a higher radius. The roughness amplitude and correlation length versus cycle number for instant frames are shown in Figure B.2b revealing the linear behavior for roughness amplitude and a non-linear behavior for correlation length. At the initial stage of roughening, the islands grow in the 2D regime (corresponding to the correlation length), and as soon as they reach the size of ca. 20 nm, their lateral size changes more slowly and they tend to grow in the 3D regime.

B.3 Curve fitting for OR charges

EquationB.1 is used to achieve the best curve fitting and the acquired coefficients are listed in Table B.1. The offset value (a) for reduction charge density is 7.8 (µC cm^{-2}) less than oxidation charge density and it can be related to the dissolution of gold in either anodic sweep[123] or reduction of gold oxide during cathodic sweep[124, 125], or in both directions[126]. The reported charge density difference per cycle in 0.5 M sulfuric acid is 4.2 (µC cm^{-2}) of which 3.7 (µC cm^{-2}) is caused by anodic sweep and 0.5 (µC cm^{-2}) by cathodic sweep[126]. The difference in offset value (a) for oxidation and reduction in our study is almost double the reported amount[126]. To have a better understanding of this happening, this difference versus cycle number is plotted in Figure B.3. This value is the highest for the first cycle and it decreases rapidly to 7 (µC cm^{-2}) and it continues to decrease over cycles. At the last cycle, it reaches 4.83 (µC cm^{-2}). This also can explain the minor difference in the logarithm coefficient (b) for oxidation and reduction in Table B.1. With the reported coefficients and the fact that there is a linear correlation between the cycle number and the surface roughness, one can relate the oxidation or reduction charge density to the roughness value.

$$y = a - b \times ln(x + c) \tag{B.1}$$

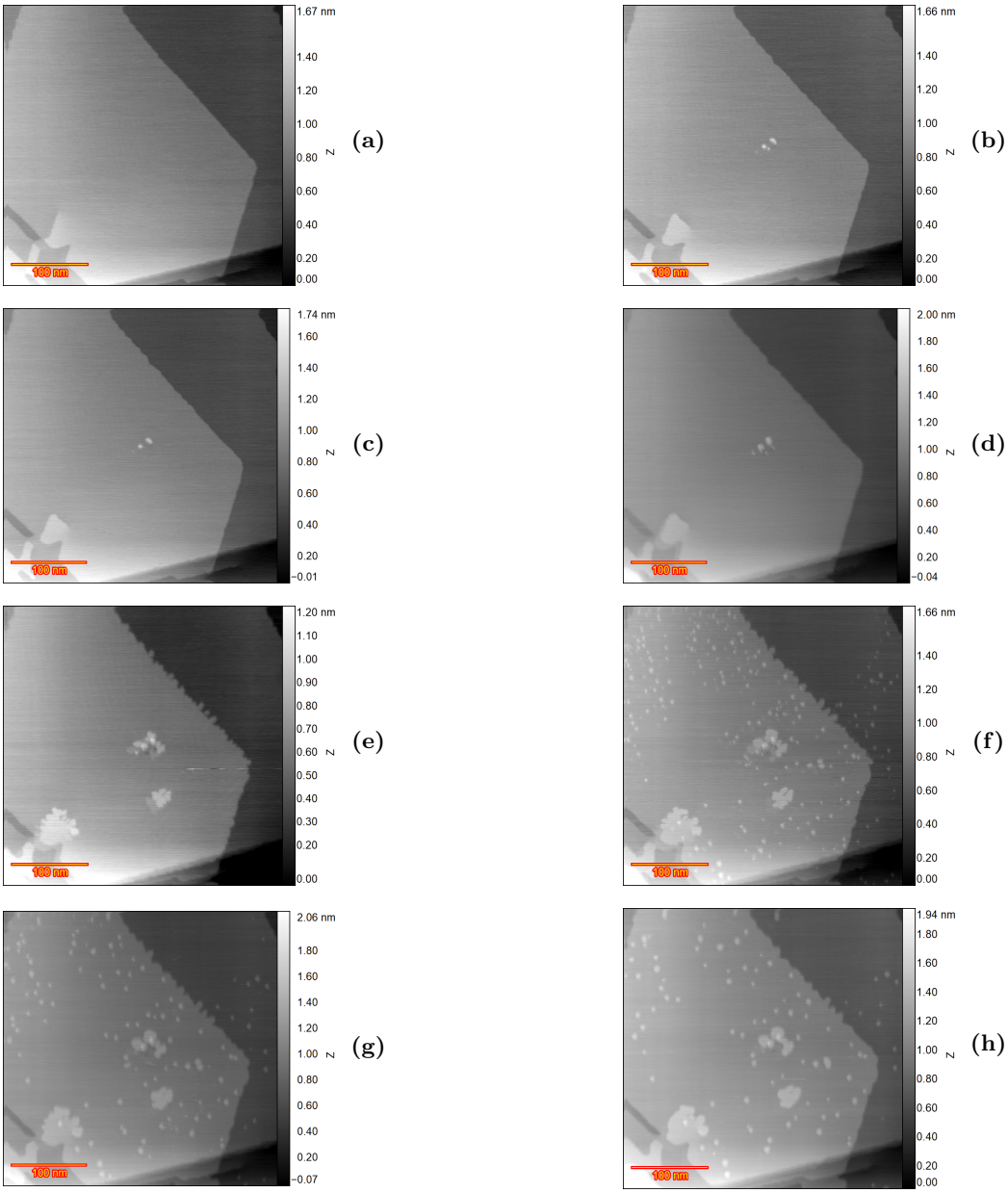

Figure B.1: Au(111) in 0.1 M sulfuric acid with the image size of 350×350 nm at different potentials a) 0, b) 0.2, c) 0.4, d) 0.6, e) 0.7, f) 0.8, g) 0.88, and h) 0.98 V versus RHE.

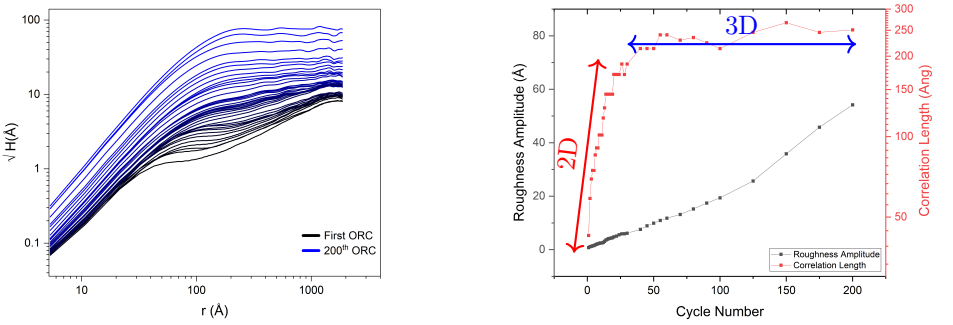

(a) **(b)**

Figure B.2: a) Height-height correlation function versus distance r for Au(111) in 0.1 M sulfuric acid as a function of the number of oxidation-reduction cycles (ORCs) for the experiment with holding potential in the double layer for the instant frames. b) Extracted roughness amplitude and correlation length versus cycle number from the HHCF results. The arrows indicate the 2D and 3D island growth regimes.

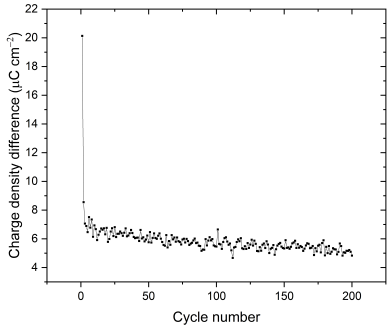

Figure B.3: Calculated the difference in oxidation-reduction charge density (µC cm^{-2}) in cyclic voltammogram of the consecutively applied 200 ORCs on Au(111) in 0.1 M H2SO4 with a scan rate of 50 mV s^{-1} versus RHE.

Table B.1: The calculated coefficients for curve-fitting on the oxidation-reduction charge density shown in Figure 9b by using EquationB.1.

Reduction Coefficients	Oxidation Coefficients
a = 561.47713 ± 0.39641	a = 569.28624 ± 0.41304
b = 5.29827 ± 0.08969	b = 5.76885 ± 0.09353
c = -0.9771 ± 0.00608	c = -0.99642 ± 9.70464E-4

B.4 Oxidation-Reduction charge density with holding the potential

Oxidation-Reduction charge density for the experiment with holding potential in the double layer is shown in Figure B.4a. In this experiment, more delays were applied, and as a result, different CVs and oxidation-reduction charge densities are expected. The amplitude of the main oxidation peak for the first and second cycles is not as noticeable as for the aforementioned results due to the applied delay. This behavior can also be seen in Figure B.4b as the charge density does not drop as fast as in other experiments. For the first twenty cycles no spike can be seen in the charge density since after each cycle the delay has been applied. However, after the twentieth cycle, the spikes appeared on the cycles subsequent to the delays. Regardless of the spikes, the general trend is an approximately logarithmic decay of the charge density over cycles.

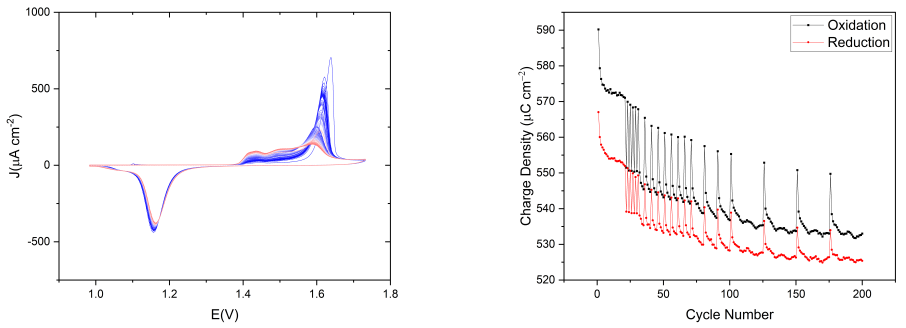

(a) **(b)**

Figure B.4: a) Cyclic voltammogram of the applied 200 ORCs on Au(111) in 0.1 M sulfuric acid with a scan rate of 50 mVs^{-1} versus RHE for the experiment with holding potential in double layer. The color gradient from blue to red corresponds to the progression from the first to the last cycle. b) Calculated oxidation-reduction charge density (µC cm^{-2}) versus the cycle number for the CVs shown in (a).

Appendix C

Supporting information for chapter 5

C.1 Au(111) in 0.1 M $HClO_4$

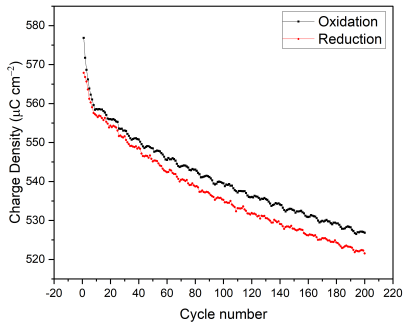

(a)

Figure C.1: Calculated oxidation and reduction charge densities for Au(111) in 0.1 M $HClO_4$ for 200 ORCs.

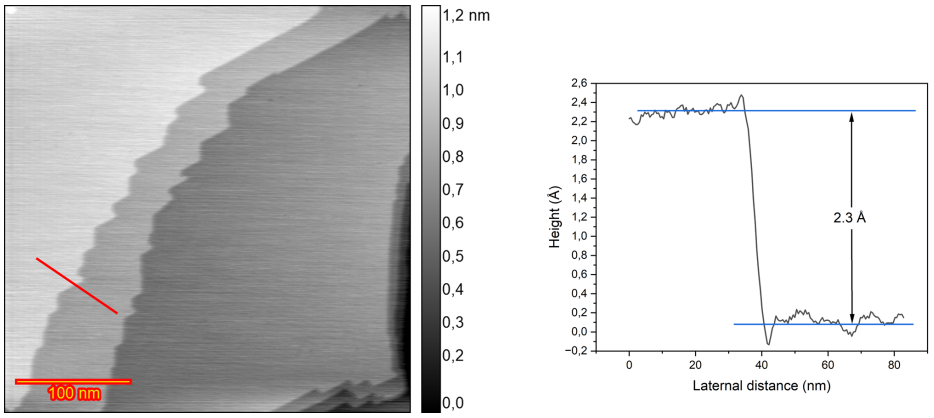

(a)

Figure C.2: EC-STM image (350×350 nm) of Au(111) in 0.1 M $HClO_4$. a) Sample surface at 0.7 V vs RHE just after annealing b) the corresponding height profile of the indicated red line in (a) that shows the step height for Au(111)

In the experiment shown in Figure C.3e-g, there is some evidence of a tip-shape effect. Thus, this effect should be considered in the discussions and conclusions for the mentioned images. However, it does not influence the final broader conclusions.

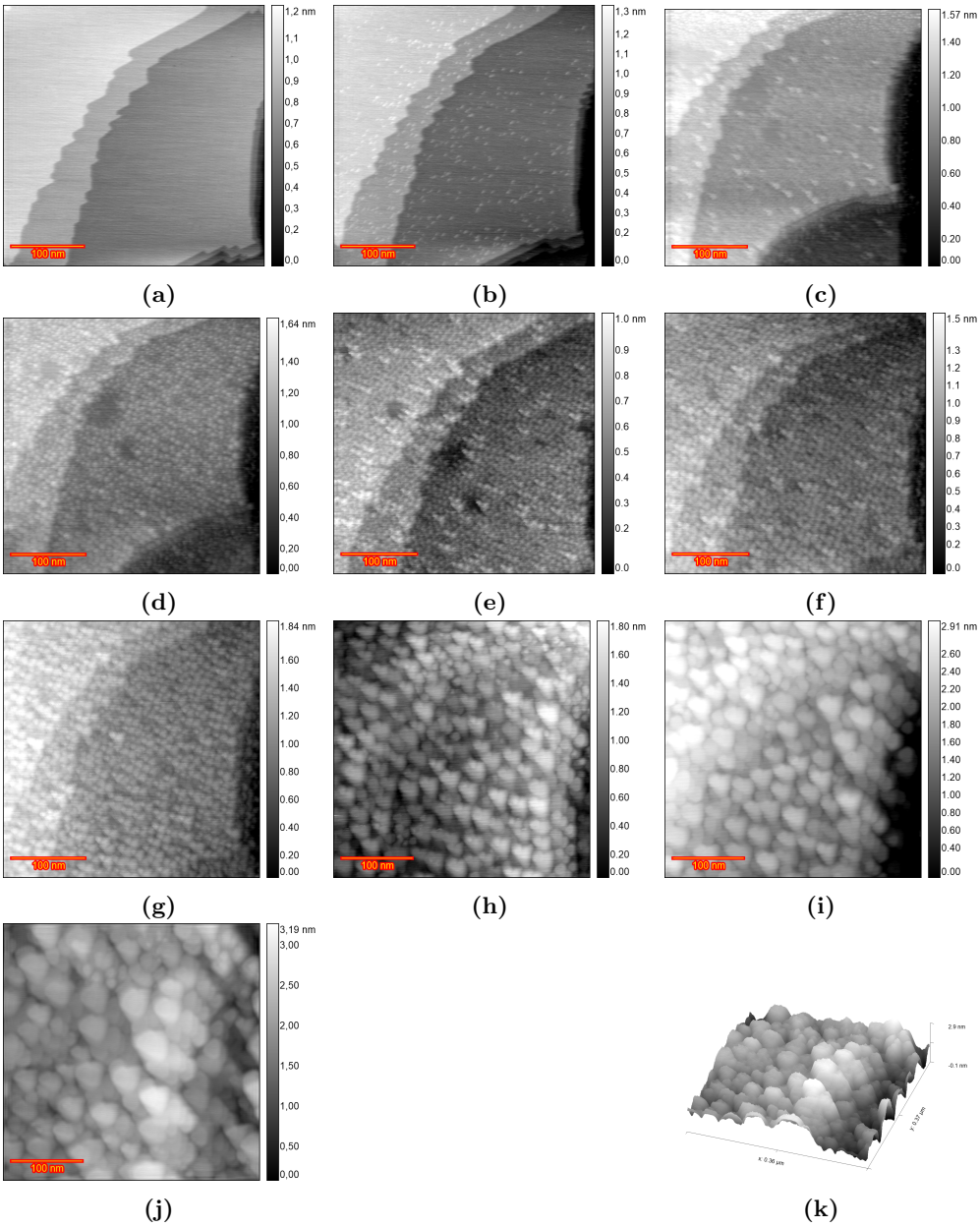

Figure C.3: EC-STM image (350×350 nm) of Au(111) in 0.1 M $HClO_4$. a) Sample surface at 0.7 V vs RHE just after annealing. b) partially lifted reconstruction at 0.9 V. c) after n ORCs from 0.9 to 1.65 V and imaging at 0.9 V n=5 d) n=15 e) n=25 f) n=40 g) n=50 h) n=110 i) n=170 j) n=200 k) 3D image after 200 ORCs.

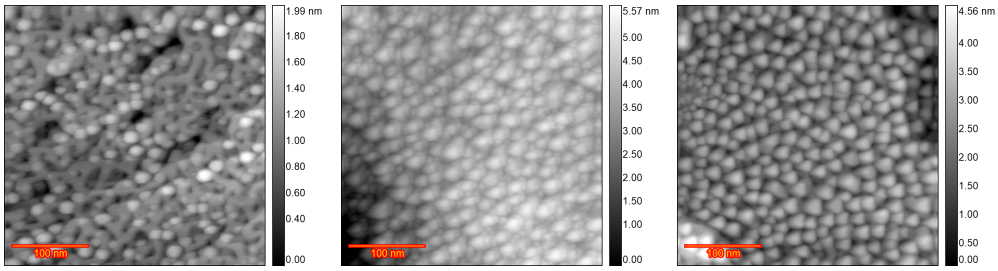

(a) **(b)** **(c)**

Figure C.4: EC-STM image (350×350 nm) of Au(111) in 0.1 M $HClO_4$ for three different experiment. a) after 200 b,c) after 70 oxidation-reduction cycle.

In the experiment shown in Figure C.6, increasing the upper potential limit to 1.8 V after the 13th ORC was tested and led to the formation of some new islands in the bottom right of the image in Figures C.6g and C.6h. This observation needs more investigation since this indicates the possibility of an unexpected inhibition of the surface oxidation reaction in these areas.

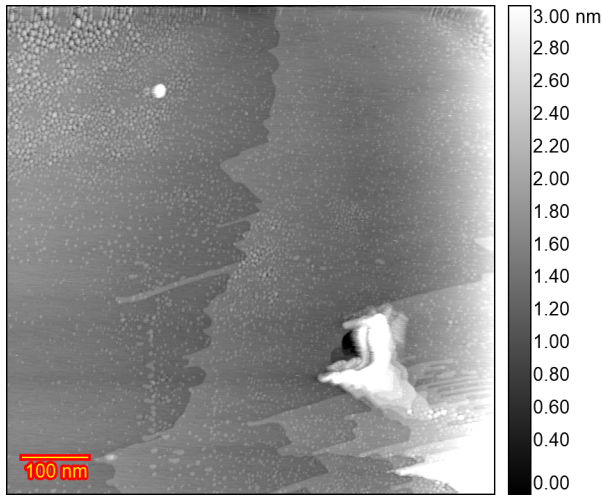

(a)

Figure C.5: EC-STM image (700×700 nm) of Au(111) in 0.1 M $HClO_4$. after 40 cycles. the surface remained largely unchanged except for a few areas.

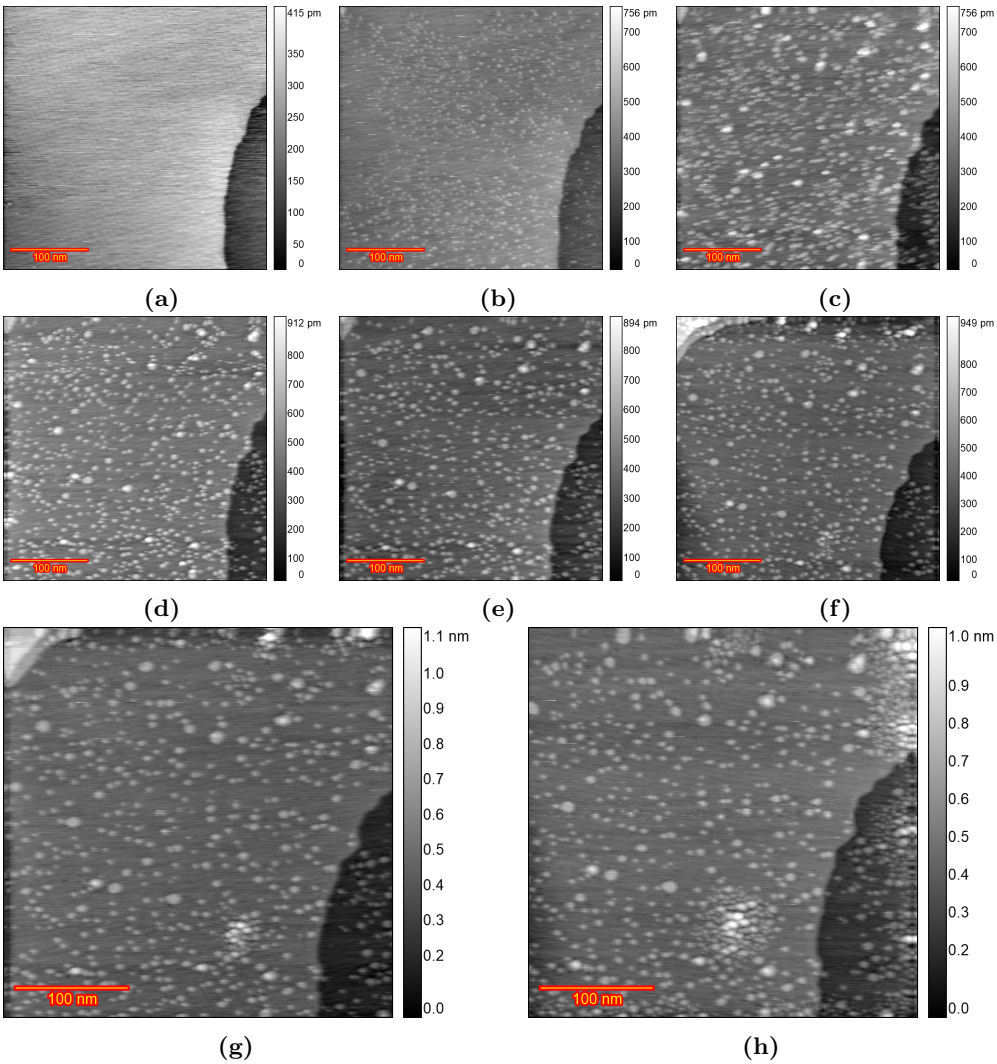

Figure C.6: EC-STM image (350×350 nm) of Au(111) in 0.1 M $HClO_4$. a) Sample surface just after annealing. b) lifted reconstruction at 0.9 V. c) after n ORCs from 0.9 to 1.65 V and imaging at 0.9 V n=1 d) n=5 e) n=13 f) n=15 g) n=20 h) n=30.

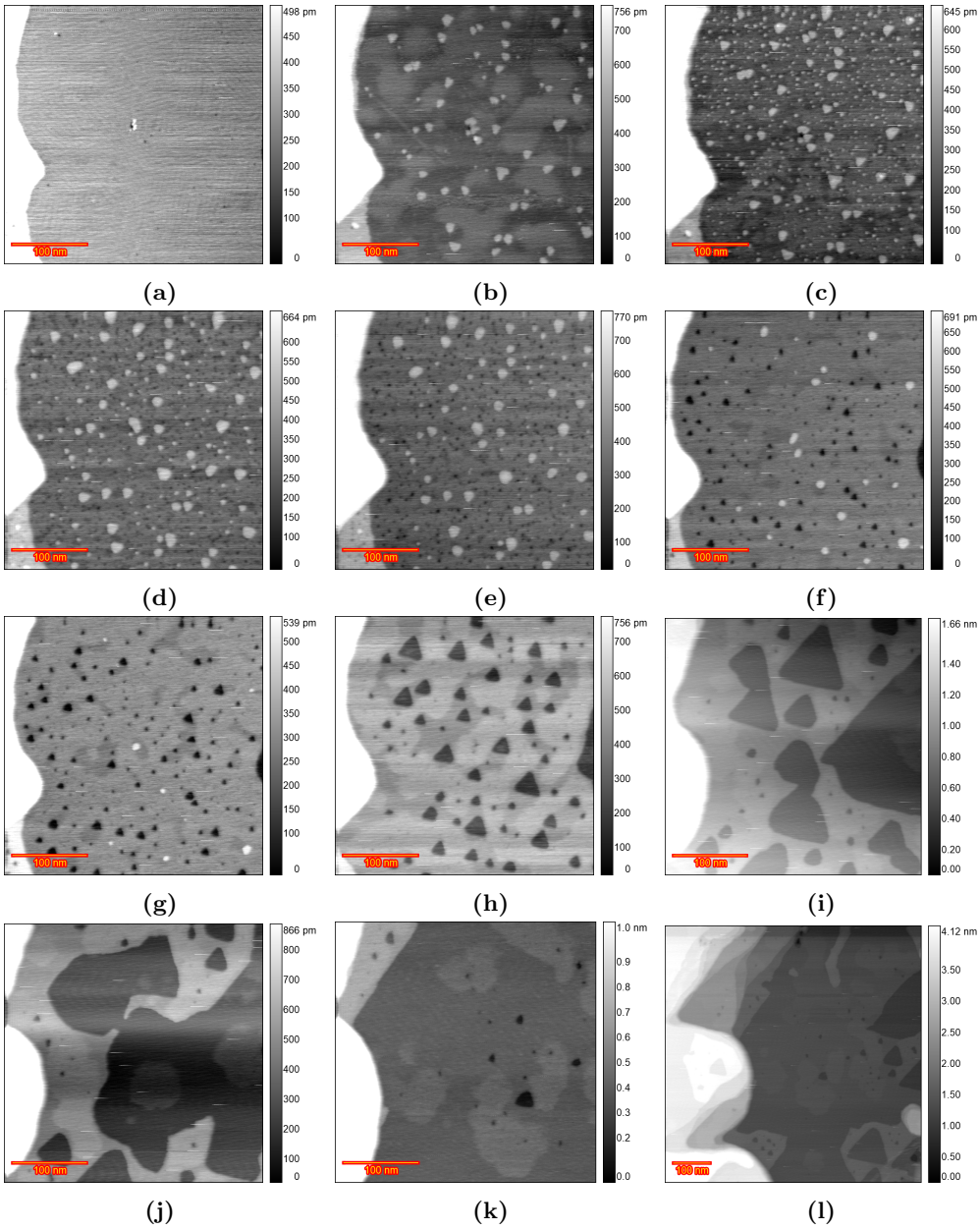

Figure C.7: EC-STM image of Au(111) in 0.1 M $HClO_4$. a) Sample surface just after annealing. b) lifted reconstruction at 0.95 V. c) after n ORCs from 0.9 to 1.65 V, n=1,d) n=5, e) n=8, f) n=15, g) n=20, h) n=50, i) n=125, j) n=150, k) n=200, l) zoomed out after 200 ORCs.

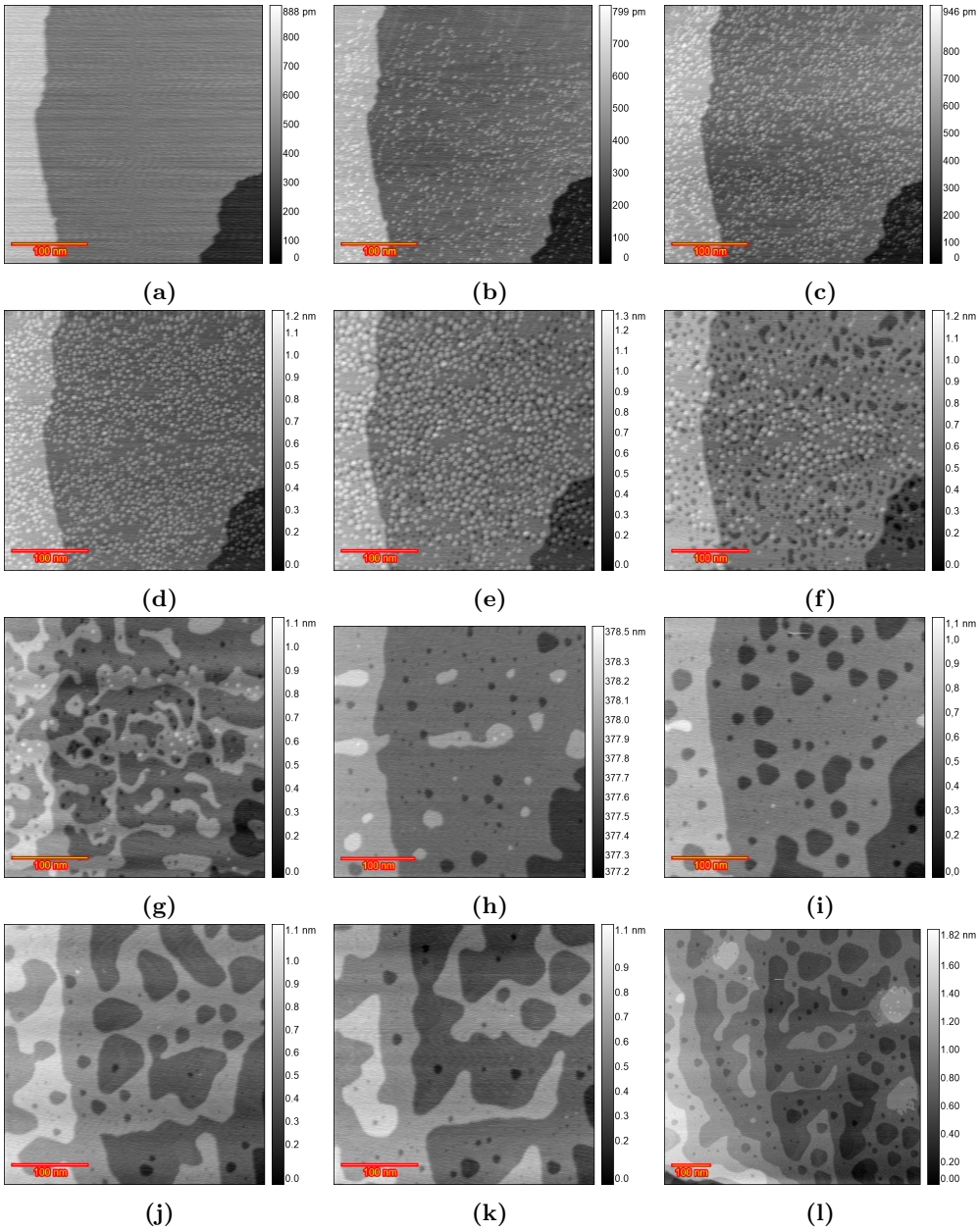

Figure C.8: EC-STM image of Au(111) in 0.1 M $HClO_4$ (ROTIPURAN), a) Sample surface just after annealing, b) lifted reconstruction at 0.9 V, c) after n ORCs from 0.9 to 1.65 V, n=2, d) n=5, e) n=20, f) n=30, g) n=50, h) n=70, i) n=100, j) n=150, k) n=175, l) n=200 zoomed out.

C.2 Au(111) in 0.1 M $HClO_4$ and 10 µM H_2SO_4

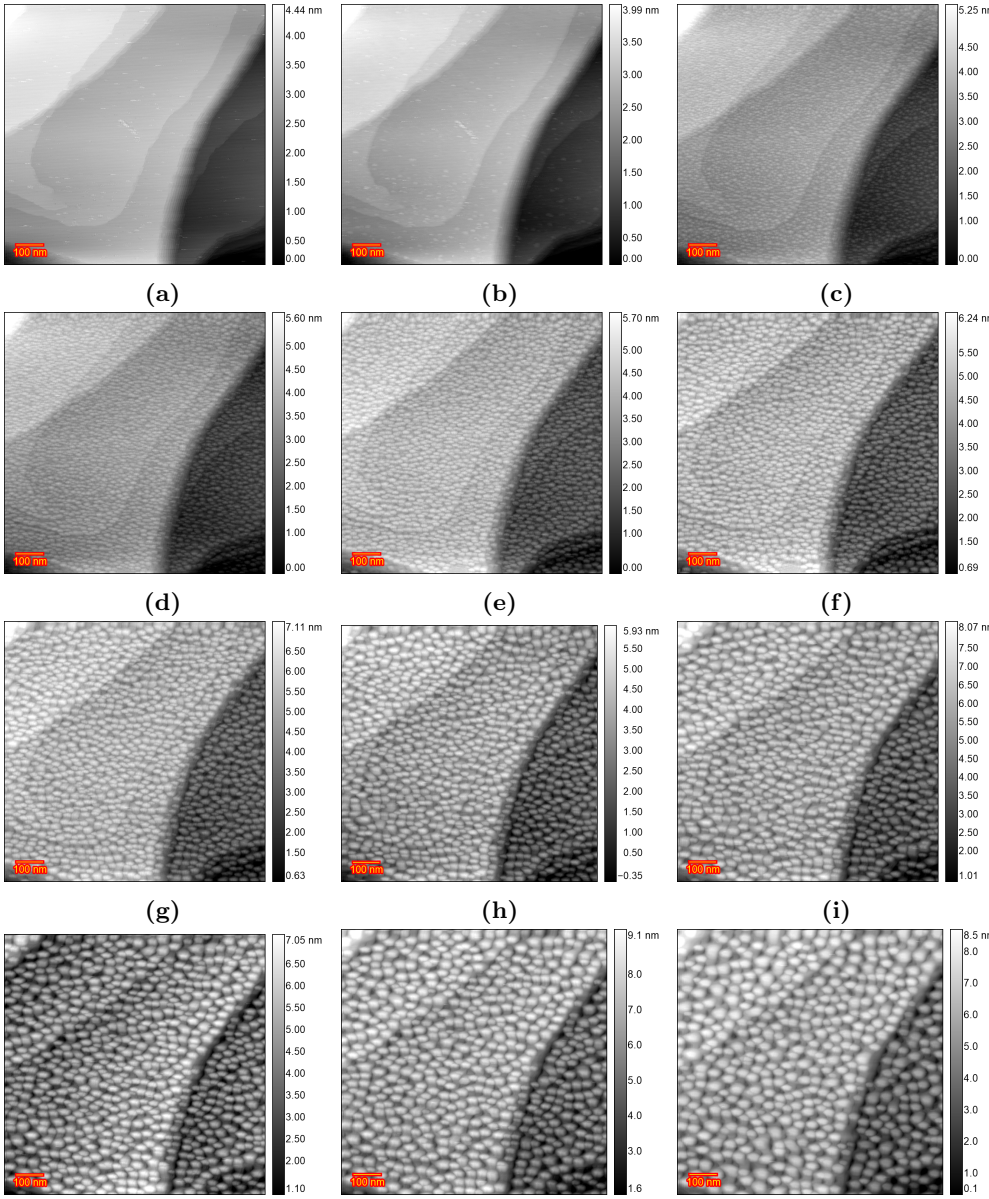

Figure C.9: EC-STM image of Au(111) in 0.1 M $HClO_4$ and 10 µM H_2SO_4, a) Sample surface just after annealing, b) lifted reconstruction at 0.9 V, c) after n ORCs from 0.8 to 1.65 V, n=10, d) n=20, e) n=35, f) n=50, g) n=75, h) n=100, i) n=125, j) n=150, k) n=175, l) n=200.

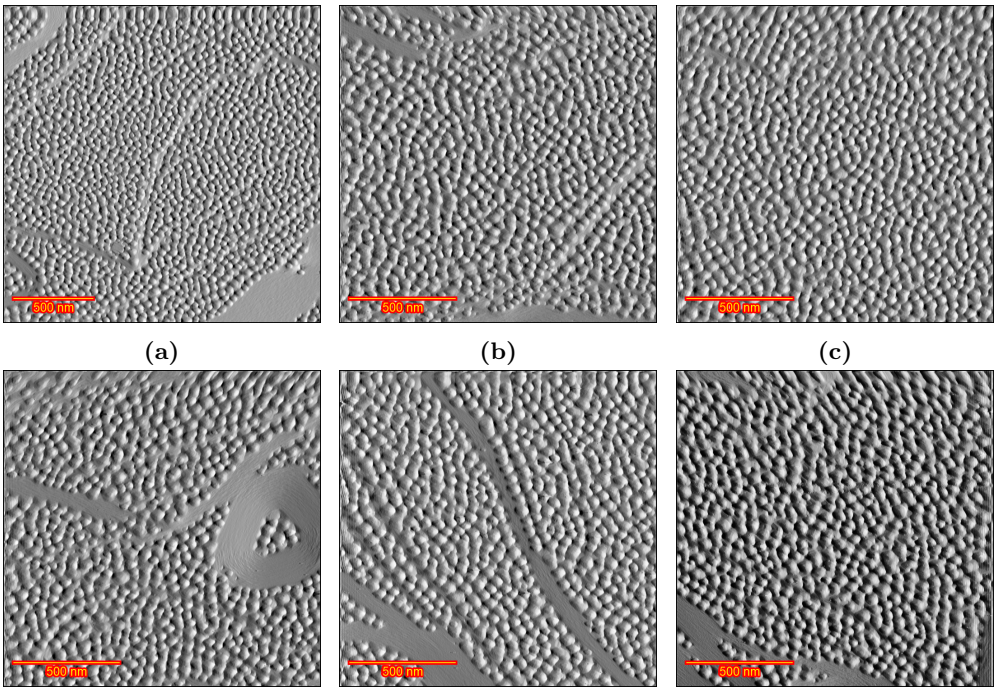

Figure C.10: Sequence of EC-STM images of Au (111) at different/random locations after 200 ORCs in 0.1 M $HClO_4$ and 10 µM H_2SO_4 in differential mode.

Figure C.11a shows the corresponding CVs of the 200 ORCs of the annealed Au (111) in a conventional electrochemical cell containing $HClO_4$ solution + 10 µM H_2SO_4, scanning from 0.9 to 1.7 V at 50 mVs^{-1} from the first cycle (in blue) to the 200th cycle (in red). Comparing the CVs after the first oxidation-reduction cycle in the H_2SO_4-containing electrolyte and pure $HClO_4$ (Figure C.11b), shows an increase in oxide formation (O4) and decrease in OH adsorption (O3) peak in the sulfate-containing solution. This can be explained by the blocking effect of absorbed sulfate on the surface at positive potentials, which blocks the chemisorption of OH^- [105, 106]. Further oxidation-reduction cycles lead to a decrease in both O4 and O3 peaks, while the O3 peak completely disappears after 200 ORCs for the sulfate containing electrolyte (Figure C.11c). The O2 and O1 peaks become more visible with the roughness increase (Figure C.11a). Figure C.11d shows oxidation reduction charge density for the 200 ORCs.

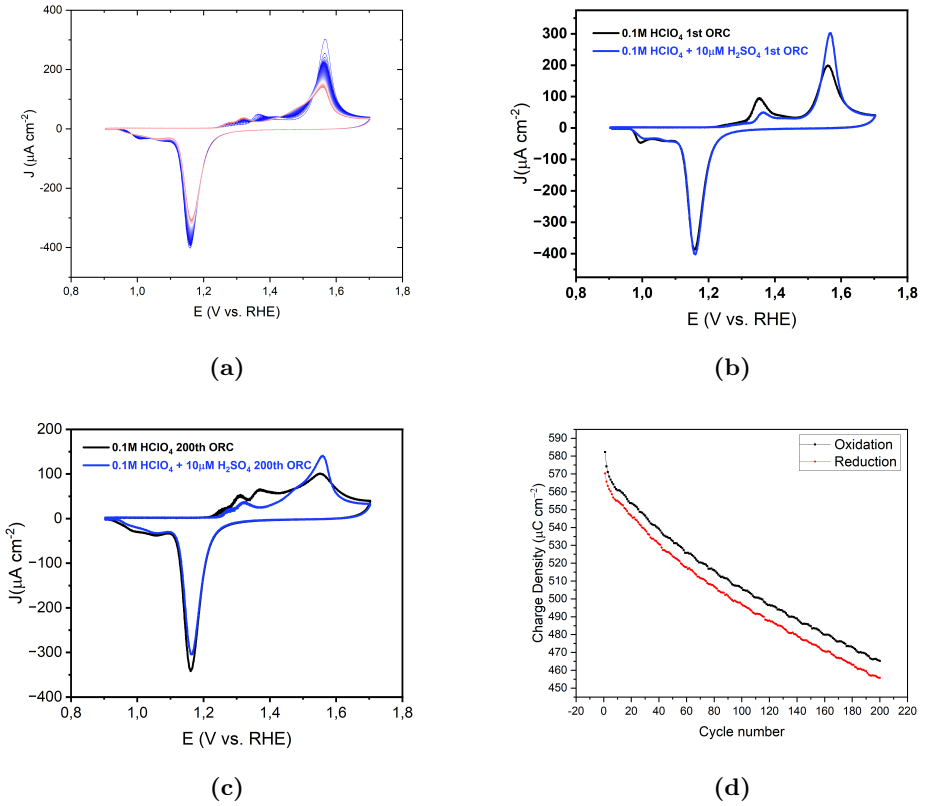

Figure C.11: CV of Au(111) in 0.1 M $HClO_4$ containing 10 µM H_2SO_4 in the potential window of 0.9 to 1.7 V versus RHE. a) All the CVs from the first (Blue) to 200th (red). b) comparison of the first CV of pure 0.1 M $HClO_4$ (black) and the electrolyte containing 10 µM H_2SO_4 (blue). c) comparison of the 200th CV of pure 0.1 M $HClO_4$ (black) and the electrolyte containing 10 µM H_2SO_4 (blue). d) Calculated oxidation and reduction charge densities for 200 ORCs.

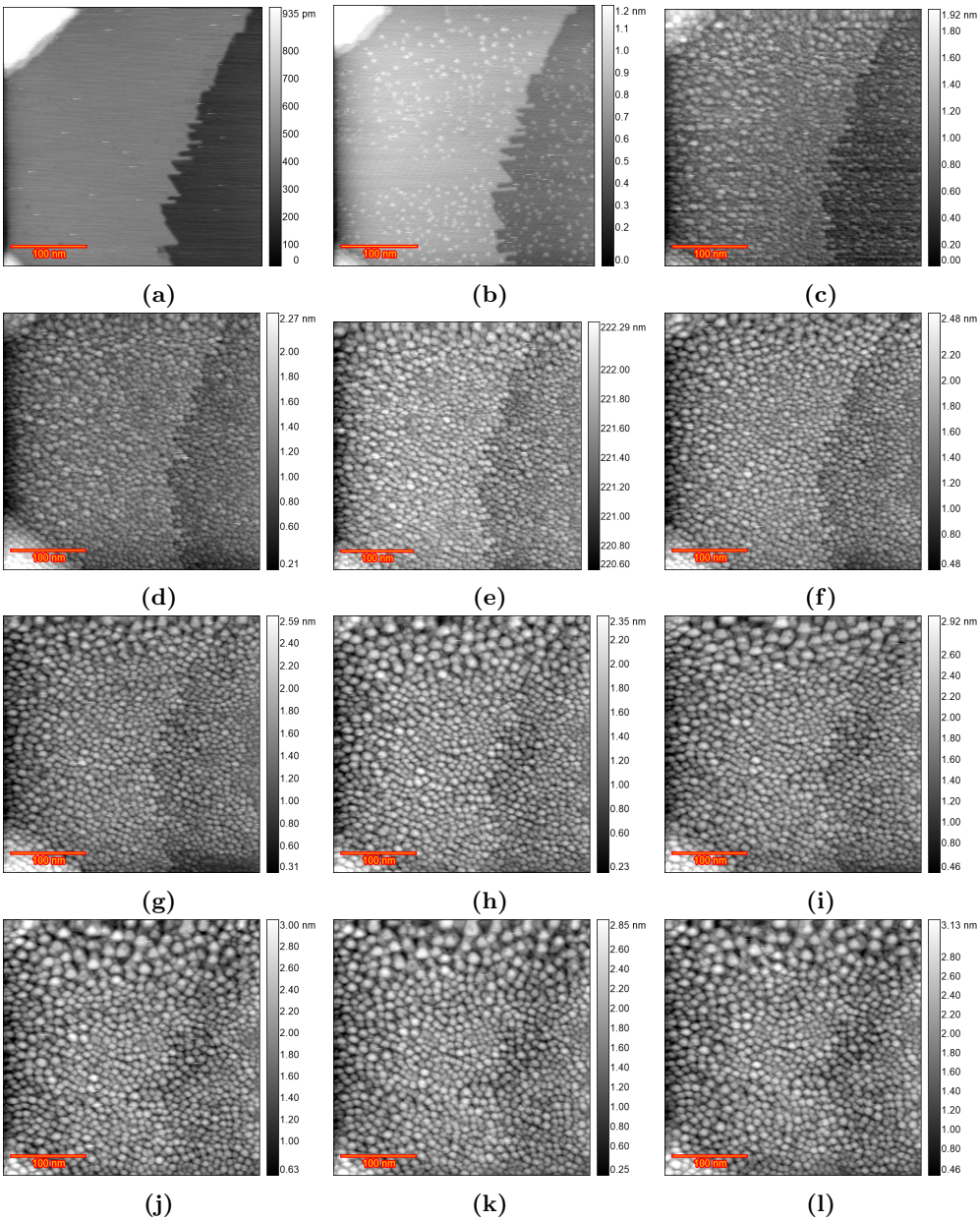

Figure C.12: Full sequence EC-STM images (350×350 nm) of experiment in 0.1 M $HClO_4$ containing 10 µM H_2SO_4. a) Sample surface just after annealing, b) lifted reconstruction at 0.9 V, c) after n ORCs from 0.8 to 1.65 V, n=10, d) n=20, e) n=35, f) n=50, g) n=75, h) n=100, i) n=125, j) n=150, k) n=175, l) n=200.

C.3 Au(111) in 0.1 M $HClO_4$ and 10 µM HCl

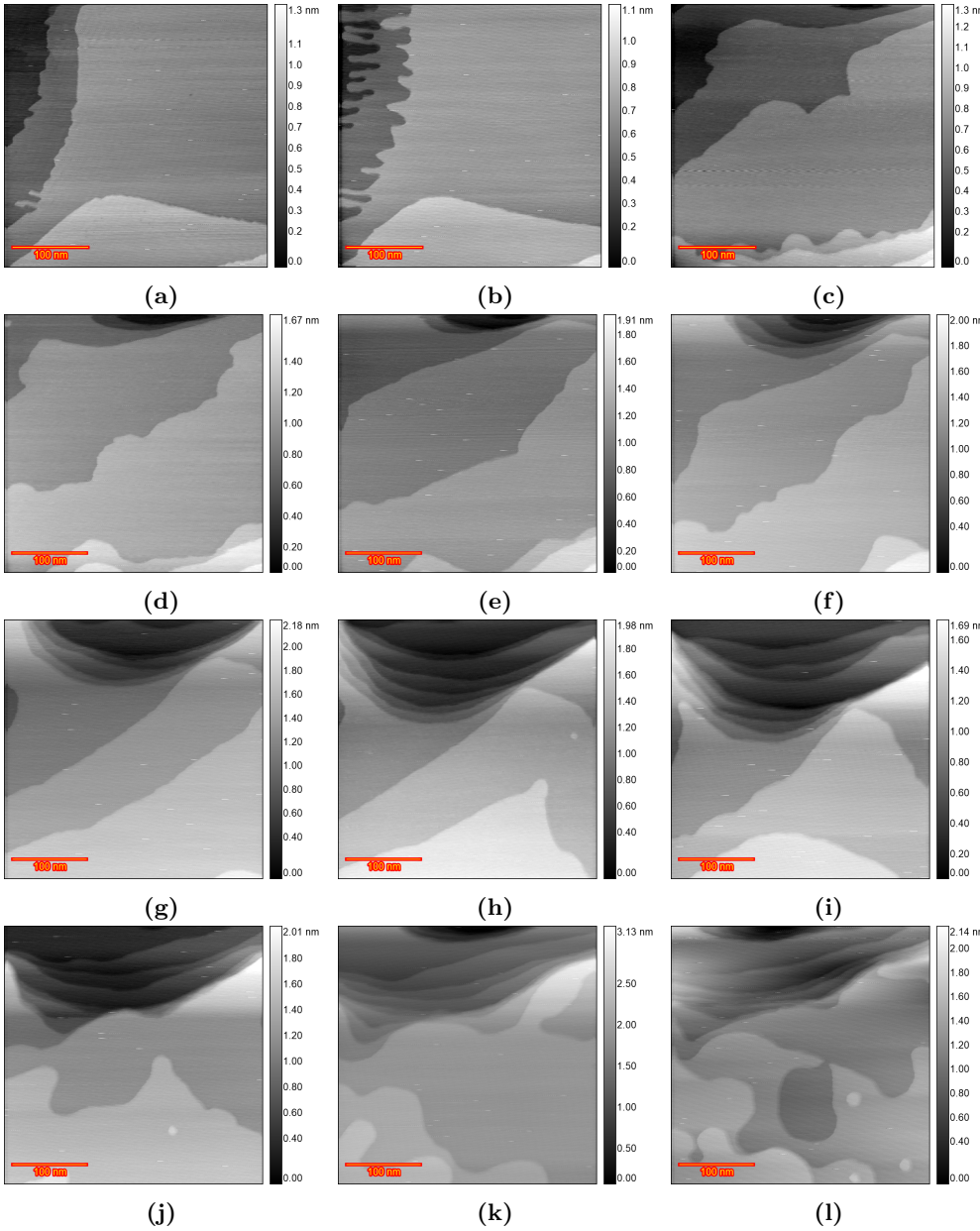

Figure C.13: Full sequence EC-STM images (350×350 nm) of experiment in 0.1 M $HClO_4$ containing 10 µM HCl. a) Sample surface just after annealing, b) lifted reconstruction at 0.9 V, c) after n ORCs from 0.8 to 1.65 V, n=10, d) n=20, e) n=35, f) n=50, g) n=75, h) n=100, i) n=125, j) n=150, k) n=175, l) n=200.

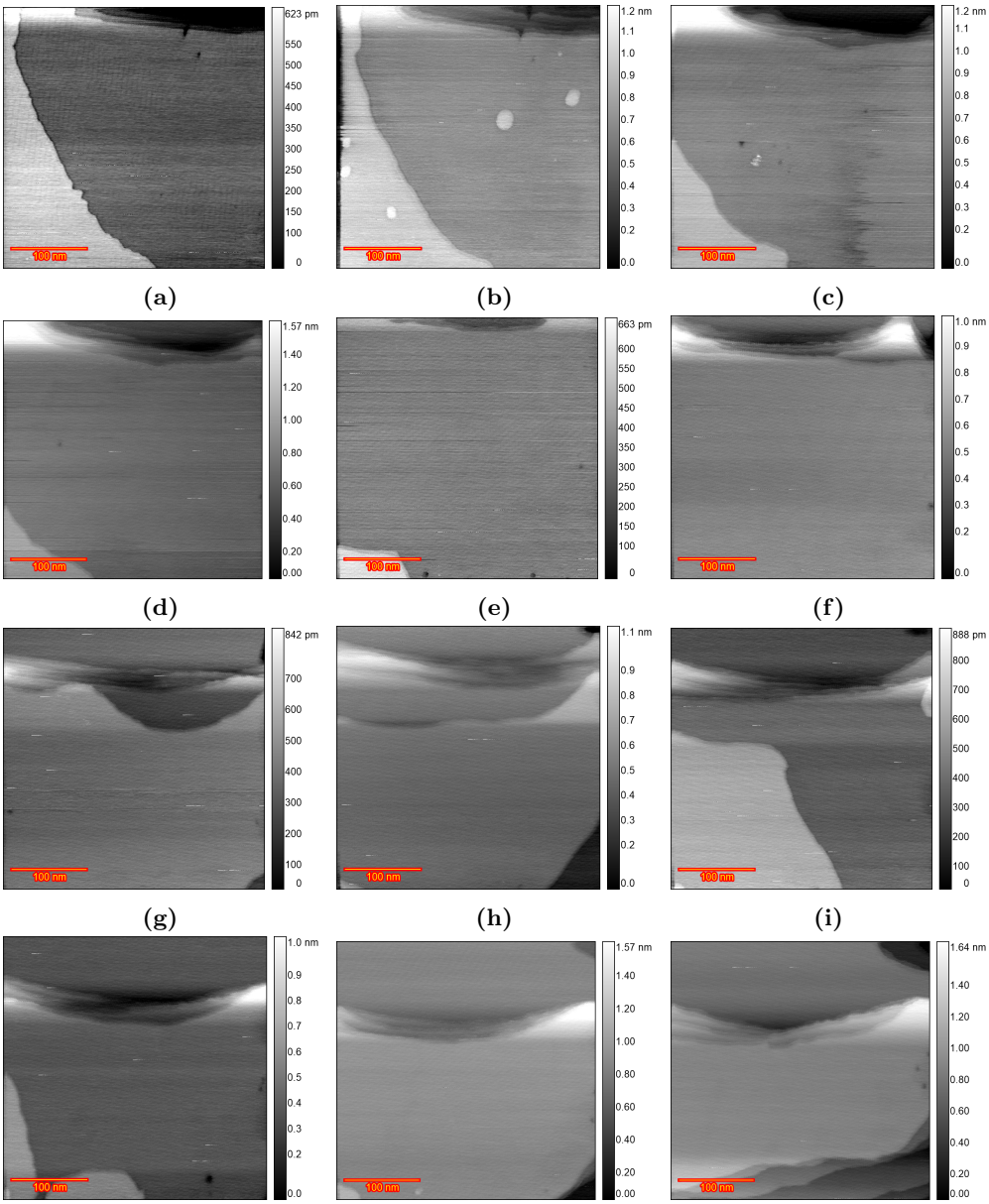

Figure C.14: Full sequence EC-STM images (350×350 nm) of experiment in 0.1 M $HClO_4$ containing 10 µM HCl. a) Sample surface just after annealing, b) lifted reconstruction at 0.9 V, c) after n ORCs from 0.8 to 1.65 V, n=10, d) n=20, e) n=35, f) n=50, g) n=75, h) n=100, i) n=125, j) n=150, k) n=175, l) n=200.

C.3. Au(111) in 0.1 M $HClO_4$ and 10 µM HCl

In a surprising discovery, repeating the experiment shown in Figure 5.8 revealed a behavior of growing vacancy islands similar to that observed in pure $HClO_4$ (experiments in Figures 5.4 and 5.5). At 0 V, terraces with a well-defined herringbone reconstruction divided by monatomic height step lines were evident (Figure C.15a). At 0.9 V, some areas showed island formation due to the lifting of the reconstruction (Figure C.15b). After performing 10 ORCs from 0.8 to 1.65 V at 50 mVs^{-1} and maintaining the potential at 0.8 V during imaging (Figure C.15c), islands disappeared and the surface was partially covered with pits and some recession was observed in the step lines, similar to our previous observations in pure $HClO_4$ (Figures 5.4 and 5.5) which were affected by impurities. Imaging after 20 ORCs (Figure C.15d) revealed the disappearance of pits and an increased recession rate of the step lines, consistent with what is expected from an $HClO_4$ solution containing Cl, as observed in Figure 5.8 . This phenomenon is likely due to the increased mobility of gold surface atoms, influenced by the greater presence of locally adsorbed Cl^- on the terraces by the experiment time. After 75 ORCs Figure C.15e shows that the step lines have receded and the terraces appear pristine. However, after 125 ORCs (Figure C.15f), some areas show pits, probably due to a lack of Cl^- ions on the newly exposed terraces following the etching of the front terrace through the receding step lines.

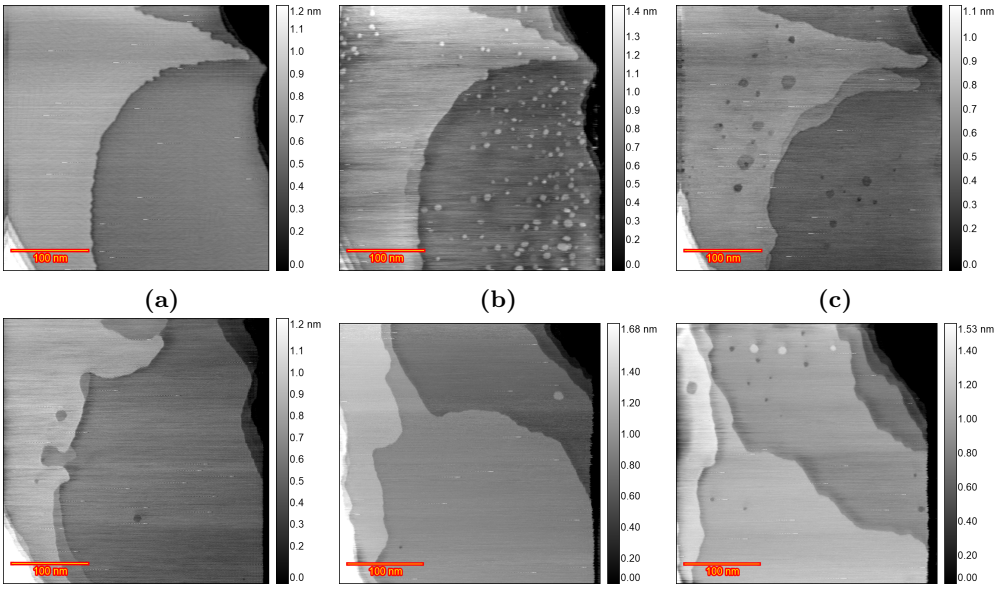

Figure C.15: EC-STM image(350×350 nm) of Au(111) in 0.1 M $HClO_4$ containing 10 µM HCl. a) Sample surface at 0.0 V vs RHE just after annealing. b) partially lifted reconstruction at 0.9 V. c) after n ORCs from 0.8 to 1.65 V and imaging at 0.8 V n=10 d) n=20 e) n=75 f) n=125.

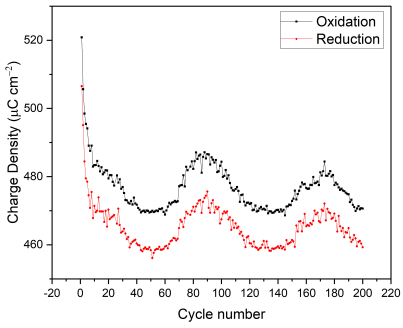

(a)

Figure C.16: Calculated oxidation and reduction charge densities of Au(111) in 0.1 M $HClO_4$ containing 10 µM HCl in the potential window of 0.9 to 1.7 V versus RHE for 200 ORCs.

C.4 Recorded CV on EC-STM

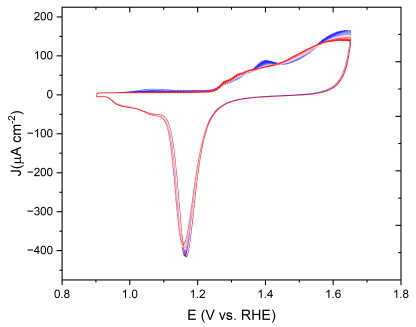

(a)

Figure C.17: Recorded CV of Au(111) in 0.1 M $HClO_4$ in the potential window of 0.9 to 1.65 V versus RHE during the EC-STM experiments in the EC-STM cell. The first CV is presented in blue and the last one is in red.

Bibliography

[1] L. Galvani. *De Viribus Electricitatis in Motu Muscolari Commentarius.* Ex Typographia Instituti Scientiarium, Bononiae,, 1791.

[2] Wolfgang Schmickler and Elizabeth Santos. *Interfacial Electrochemistry.* Springer Berlin Heidelberg, Berlin, Heidelberg, 2010.

[3] Larry R. Faulkner Allen J. Bard. *Electrochemical Methods: Fundamentals and Applications, 2nd Edition*, volume 677. Wiley; 2nd edition, 2004.

[4] Dieter M. Kolb. Electrochemical Surface Science. *Angewandte Chemie International Edition*, 40(7):1162–1181, apr 2001.

[5] Xiaoting Chen and Marc T. M. Koper. In situ ec-afm study of the initial stages of cathodic corrosion of pt(111) and polycrystalline pt in acid solution. *The Journal of Physical Chemistry Letters*, 14(21):4997–5003, 2023. PMID: 37222413.

[6] Carsten Köntje, Dieter M. Kolb, and Gregory Jerkiewicz. Roughening and long-range nanopatterning of au(111) through potential cycling in aqueous acidic media. *Langmuir*, 29:10272–10278, 8 2013.

[7] Georg H. Simon, Christopher S. Kley, and Beatriz Roldan Cuenya. Potential-dependent morphology of copper catalysts during co2 electroreduction revealed by in-situ atomic force microscopy. *Angewandte Chemie International Edition*, 60(5):2561–2568, 2021.

[8] Toshihiro Kondo, Jun Morita, Kazuya Hanaoka, Satoru Takakusagi, Kazuhisa Tamura, Masamitu Takahasi, Jun'ichiro Mizuki, and Kohei Uosaki. Structure of Au(111) and Au(100) Single-Crystal Electrode Surfaces at Various Potentials in Sulfuric Acid Solution Determined by In Situ Surface X-ray Scattering. *The Journal of Physical Chemistry C*, 111(35):13197–13204, sep 2007.

[9] Hassan Javed, Kees Kolmeijer, Nick Klein, Jamie A. Trindell, Gregory Schneider, and Rik V. Mom. A laboratory-based electrochemical nap-xps system for operando electrocatalysis studies. *Vacuum*, 231:113755, 2025.

[10] G Binning, H Rohrer, Ch Gerber, and E Weibel. Surface Studies by Scanning Tunneling Microscopy. *Phys. Rev*, 49(1):57, 1982.

[11] G. Binnig, H. Rohrer, Ch Gerber, and E. Weibel. Tunneling through a controllable vacuum gap. *Applied Physics Letters*, 40(2):178–180, jan 1982.

[12] W. Ho. Single-molecule chemistry. *The Journal of Chemical Physics*, 117(24):11033–11061, dec 2002.

[13] Harold J.W. Zandvliet and Arie van Houselt. Scanning Tunneling Spectroscopy. *Annual Review of Analytical Chemistry*, 2(1):37–55, jul 2009.

[14] D. M. Eigler and E. K. Schweizer. Positioning single atoms with a scanning tunnelling microscope. *Nature*, 344(6266):524–526, apr 1990.

[15] C. Julian Chen. *Introduction to Scanning Tunneling Microscopy*. Oxford University PressOxford, third edition, mar 2021.

[16] Milutin Stanacevic, Kartikeya Murari, Abhishek Rege, Gert Cauwenberghs, and Nitish V. Thakor. VLSI Potentiostat Array With Oversampling Gain Modulation for Wide-Range Neurotransmitter Sensing. *IEEE Transactions on Biomedical Circuits and Systems*, 1(1):63–72, mar 2007.

[17] B Drake, R. Sonnenfeld, J. Schneir, and P.K. Hansma. Scanning tunneling microscopy of processes at liquid-solid interfaces. *Surface Science*, 181(1-2):92–97, mar 1987.

[18] J. V. Barth, H. Brune, G. Ertl, and R. J. Behm. Scanning tunneling microscopy observations on the reconstructed Au(111) surface: Atomic structure, long-range superstructure, rotational domains, and surface defects. *Physical Review B*, 42(15):9307–9318, nov 1990.

[19] U. Harten, A. M. Lahee, J. Peter Toennies, and Ch. Wöll. Observation of a Soliton Reconstruction of Au(111) by High-Resolution Helium-Atom Diffraction. *Physical Review Letters*, 54(24):2619–2622, jun 1985.

[20] M Schneeweiss. Oxide formation on Au(111) an in situ STM study. *Solid State Ionics*, 94(1-4):171–179, feb 1997.

[21] B.E. Conway. Electrochemical oxide film formation at noble metals as a surface-chemical process. *Progress in Surface Science*, 49(4):331–452, aug 1995.

[22] Marie Anne Schneeweiss, Dieter M. Kolb, Dezhong Liu, and Daniel Mandler. Anodic oxidation of Au(111). *Canadian Journal of Chemistry*, 75(11):1703–1709, nov 1997.

[23] Fernando Silva, Cosme Moura, and A. Hamelin. Formation of a monolayer of oxide on gold single crystal face electrodes in sulphamic acid solutions. *Electrochimica Acta*, 34(12):1665–1671, dec 1989.

[24] Oscar Diaz-Morales, Federico Calle-Vallejo, Casper de Munck, and Marc T M Koper. Electrochemical water splitting by gold: evidence for an oxide decomposition mechanism. *Chemical Science*, 4(6):2334, 2013.

[25] S. Bourkane, C. Gabrielle, F. Huet, and M. Keddam. Investigation of gold oxidation in sulfuric medium—I. Electrochemical impedance techniques. *Electrochimica Acta*, 38(7):1023–1028, may 1993.

[26] Ping Gao, David Gosztola, Lam-Wing H Leung, and Michael J Weaver. Surface-enhanced Raman scattering at gold electrodes: dependence on electrochemical pretreatment conditions and comparisons with silver. *Journal of Electroanalytical Chemistry and Interfacial Electrochemistry*, 233(1-2):211–222, sep 1987.

[27] Karrie J. Hanson and Michael P. Green. Electrochemical Roughening and Annealing of Au(111) Surfaces in Perchloric and Sulfuric Acid Electrolytes Studied by STM. *MRS Proceedings*, 237(111):323, feb 1991.

[28] Andrzej Wieckowski. *Interfacial Electrochemistry*. Routledge, nov 2017.

[29] Johannes M. Hermann, Areeg Abdelrahman, Timo Jacob, and Ludwig A. Kibler. Potential-dependent reconstruction kinetics probed by HER on Au(111) electrodes. *Electrochimica Acta*, 347:136287, jul 2020.

[30] Shengxiang Yang and Dennis G. H. Hetterscheid. Redefinition of the Active Species and the Mechanism of the Oxygen Evolution Reaction on Gold Oxide. *ACS Catalysis*, 10(21):12582–12589, nov 2020.

[31] G. Palasantzas and J. Krim. Effect of the form of the height-height correlation function on diffuse x-ray scattering from a self-affine surface. *Physical Review B*, 48(5):2873–2877, aug 1993.

[32] J. Krim and J. O. Indekeu. Roughness exponents: A paradox resolved. *Physical Review E*, 48(2):1576–1578, aug 1993.

[33] A. Le Gal and M. Klüppel. Investigation and modelling of rubber stationary friction on rough surfaces. *Journal of Physics: Condensed Matter*, 20(1):015007, jan 2008.

[34] Pai Li and Feng Ding. Origin of the herringbone reconstruction of Au(111) surface at the atomic scale. *Science Advances*, 8(40):1–8, oct 2022.

[35] M. Giesen, G. Schulze Icking-Konert, and H. Ibach. Fast Decay of Adatom Islands and Mounds on Cu(111): A New Effective Channel for Interlayer Mass Transport. *Physical Review Letters*, 80(3):552–555, jan 1998.

[36] M. Giesen, G. Schulze Icking-Konert, and H. Ibach. Interlayer Mass Transport and Quantum Confinement of Electronic States. *Physical Review Letters*, 82(15):3101–3104, apr 1999.

[37] Margret Giesen and Harald Ibach. On the mechanism of rapid mound decay. *Surface Science*, 464(1):L697–L702, sep 2000.

[38] David Nečas and Petr Klapetek. Gwyddion: an open-source software for SPM data analysis. *Open Physics*, 10(1):181–188, feb 2012.

[39] Wei Wang, Yi-Fan Huang, Dong-Yu Liu, Fang-Fang Wang, Zhong-Qun Tian, and Dongping Zhan. Electrochemically roughened gold microelectrode for surface-enhanced Raman spectroscopy. *Journal of Electroanalytical Chemistry*, 779:126–130, oct 2016.

[40] Ulmas Zhumaev, Alexander V. Rudnev, Jian-Feng Li, Akiyoshi Kuzume, Thu-Hien Vu, and Thomas Wandlowski. Electro-oxidation of au(111) in contact with aqueous electrolytes: New insight from in situ vibration spectroscopy. *Electrochimica Acta*, 112:853–863, 2013.

[41] Leon Jacobse, Yi-Fan Huang, Marc T. M. Koper, and Marcel J. Rost. Correlation of surface site formation to nanoisland growth in the electrochemical roughening of Pt(111). *Nature Materials*, 17(3):277–282, mar 2018.

[42] Marcel J Rost, Leon Jacobse, and Marc T M Koper. The dualism between adatom- and vacancy-based single crystal growth models. *Nature Communications*, 10(1):5233, 2019.

[43] J. V. Barth, H. Brune, G. Ertl, and R. J. Behm. Scanning tunneling microscopy observations on the reconstructed au(111) surface: Atomic structure, long-range superstructure, rotational domains, and surface defects. *Phys. Rev. B*, 42:9307–9318, Nov 1990.

[44] U. Harten, A. M. Lahee, J. Peter Toennies, and Ch. Wöll. Observation of a soliton reconstruction of au(111) by high-resolution helium-atom diffraction. *Phys. Rev. Lett.*, 54:2619–2622, Jun 1985.

[45] Carsten Koentje, Dieter Kolb, and Gregory Jerkiewicz. Roughening and long-range nanopatterning of au(111) through potential cycling in aqueous acidic media. *Langmuir : the ACS journal of surfaces and colloids*, 29, 07 2013.

[46] M.A. Schneeweiss and D.M. Kolb. Oxide formation on au(111) an in situ stm study. *Solid State Ionics*, 94(1):171–179, 1997. Papers from the International Workshop.

[47] Benchaporn Lertanantawong, Anthony P. O'Mullane, Werasak Surareungchai, Mithran Somasundrum, L. Declan Burke, and Alan M. Bond. Study of the underlying electrochemistry of polycrystalline gold electrodes in aqueous solution and electrocatalysis by large amplitude fourier transformed alternating current voltammetry. *Langmuir*, 24(6):2856–2868, 2008. PMID: 18266392.

[48] B.E. Conway. Electrochemical oxide film formation at noble metals as a surface-chemical process. *Progress in Surface Science*, 49(4):331–452, 1995.

[49] Oscar Diaz-Morales, Federico Calle-Vallejo, Casper de Munck, and Marc T. M. Koper. Electrochemical water splitting by gold: evidence for an oxide decomposition mechanism. *Chem. Sci.*, 4:2334–2343, 2013.

[50] Saeid Behjati and Marc T. M. Koper. In situ stm study of roughening of au(111) single-crystal electrode in sulfuric acid solution during oxidation–reduction cycles. *The Journal of Physical Chemistry C*, 128(44):19024–19034, 2024.

[51] M.A. Diaz, G.H. Kelsall, and N.J. Welham. Electrowinning coupled to gold leaching by electrogenerated chlorine. au(iii) au(i) au kinetics in aqueous cl2/cl-electrolytes. *Journal of Electroanalytical Chemistry*, 361(1):25–38, 1993. An International Journal Devoted to all Aspects of Electrode Kinetics, Interfacial Structure, Properties of Electrolytes, Colloid and Biological Electrochemistry.

[52] Shen Ye, Chikara Ishibashi, Katsuaki Shimazu, and Kohei Uosaki. An in situ electrochemical quartz crystal microbalance study of the dissolution process of a gold electrode in perchloric acid solution containing chloride ion. *Journal of The Electrochemical Society*, 145(5):1614, may 1998.

[53] Th. Heumann and H. S. Panesar. Beitrag zur frage nach dem auflösungsmechanismus von gold zu chlorkomplexen und nach seiner passivierung. *Zeitschrift für Physikalische Chemie*, 229O:84–97, 5 1965.

[54] Shen Ye, Chikara Ishibashi, and Kohei Uosaki. Anisotropic dissolution of an au(111) electrode in perchloric acid solution containing chloride anion investigated by in situ stmthe important role of adsorbed chloride anion. *Langmuir*, 15(3):807–812, 1999.

[55] Dennis J. Trevor, Christopher E. D. Chidsey, and Dominic N. Loiacono. In situ scanning-tunneling-microscope observation of roughening, annealing, and dissolution of gold (111) in an electrochemical cell. *Phys. Rev. Lett.*, 62:929–932, Feb 1989.

[56] Margret Giesen and Dieter M. Kolb. Influence of anion adsorption on the step dynamics on Au (111) electrodes. *Surface Science*, 468(1-3):149–164, nov 2000.

[57] Dennis J Trevor, Christopher ED Chidsey, and Dominic N Loiacono. In situ scanning-tunneling-microscope observation of roughening, annealing, and dissolution of gold (111) in an electrochemical cell. *Physical review letters*, 62(8):929, 1989.

[58] Karina Morgenstern, Georg Rosenfeld, Bene Poelsema, and George Comsa. Brownian motion of vacancy islands on ag (111). *Physical review letters*, 74(11):2058, 1995.

[59] M Eßer, K Morgenstern, G Rosenfeld, and G Comsa. Dynamics of vacancy island coalescence on ag (111). *Surface science*, 402:341–345, 1998.

[60] Cristina Vaz-Dominguez, Asier Aranzabal, and Angel Cuesta. In situ stm observation of stable dislocation networks during the initial stages of the lifting of the reconstruction on au (111) electrodes. *The Journal of Physical Chemistry Letters*, 1(14):2059–2062, 2010.

[61] V Maurice, H-H Strehblow, and P Marcus. In situ stm study of the initial stages of oxidation of cu (111) in aqueous solution. *Surface Science*, 458(1-3):185–194, 2000.

[62] Carissima M Vitus and Alison J Davenport. In situ scanning tunneling microscopy studies of the formation and reduction of a gold oxide monolayer on au (111). *Journal of The Electrochemical Society*, 141(5):1291, 1994.

[63] Monika M Biener, Juergen Biener, and Cynthia M Friend. Revisiting the s- au (111) interaction: Static or dynamic? *Langmuir*, 21(5):1668–1671, 2005.

[64] Monika M Biener, Juergen Biener, and Cynthia M Friend. Sulfur-induced mobilization of au surface atoms on au (1 1 1) studied by real-time stm. *Surface science*, 601(7):1659–1667, 2007.

[65] BK Min, AR Alemozafar, MM Biener, J Biener, and CM Friend. Reaction of au (111) with sulfur and oxygen: Scanning tunneling microscopic study. *Topics in Catalysis*, 36:77–90, 2005.

[66] Holly Walen, Da-Jiang Liu, Junepyo Oh, Hyunseob Lim, James W Evans, Yousoo Kim, and PA Thiel. Self-organization of s adatoms on au (111): sqrt3r30 rows at low coverage. *The Journal of chemical physics*, 143(1), 2015.

[67] Peter M Spurgeon, Da-Jiang Liu, Theresa L Windus, James W Evans, and Patricia A Thiel. Enhanced nanostructure dynamics on au (111) with adsorbed sulfur due to au- s complex formation. *ChemPhysChem*, 22(4):349–358, 2021.

[68] Patricia A Thiel, Mingmin Shen, Da-Jiang Liu, and James W Evans. Adsorbate-enhanced transport of metals on metal surfaces: Oxygen and sulfur on coinage metals. *Journal of Vacuum Science & Technology A*, 28(6):1285–1298, 2010.

[69] W. L. Ling, N. C. Bartelt, K. Pohl, J. de la Figuera, R. Q. Hwang, and K. F. McCarty. Enhanced self-diffusion on cu(111) by trace amounts of s: Chemical-reaction-limited kinetics. *Phys. Rev. Lett.*, 93:166101, Oct 2004.

[70] Nicci Fröhlich, Julia Fernández-Vidal, Francesc Valls Mascaró, Arthur J. Shih, Mingchuan Luo, and Marc T.M. Koper. Effect of trace impurities in perchloric acid on blank voltammetry of pt(111). *Electrochimica Acta*, 466:143035, 2023.

[71] L. D. Burke and P. F. Nugent. The electrochemistry of gold: I. the redox behaviour of the metal in aqueous media. *Gold Bulletin*, 30:43–53, 1997.

[72] Fritz Scholz. Electroanalytical methods: Guide to experiments and applications. *Electroanalytical Methods: Guide to Experiments and Applications*, pages 1–359, 2010.

[73] L. M. Siperko, S. S. Hurban, J. M. Spalik, and A. D. Katnani. Complementary scanning tunneling microscopy and scanning electron microscopy studies of electroplated gold surfaces. *Journal of Vacuum Science and Technology A*, 10:2400–2403, 7 1992.

[74] C. Bocking and I. R. Christie. Gold electroplating a brief overview. *Interdisciplinary Science Reviews*, 17:239–243, 1992.

[75] Aimin Yu, Zhijian Liang, Jinhan Cho, and Frank Caruso. Nanostructured electrochemical sensor based on dense gold nanoparticle films. *Nano Letters*, 3:1203–1207, 9 2003.

[76] Paramaconi Rodriguez and Marc T. M. Koper. Electrocatalysis on gold. *Phys. Chem. Chem. Phys.*, 16:13583–13594, 2014.

[77] J. Zhang, K. Sasaki, E. Sutter, and R. R. Adzic. Stabilization of platinum oxygen-reduction electrocatalysts using gold clusters. *Science*, 315:220–222, 1 2007.

[78] Marc T.M. Koper and Hendrik A. Heering. Comparison of electrocatalysis and bioelectrocatalysis of hydrogen and oxygen redox reactions. *Fuel Cell Science: Theory, Fundamentals, and Biocatalysis*, pages 71–110, 10 2010.

[79] Sang Hoon Kim. Nanoporous gold for energy applications. *The Chemical Record*, 21:1199–1215, 5 2021.

[80] Yi Chun Lu, Zhichuan Xu, Hubert A. Gasteiger, Shuo Chen, Kimberly Hamad-Schifferli, and Yang Shao-Horn. Platinum-gold nanoparticles: A highly active bifunctional electrocatalyst for rechargeable lithium-air batteries. *Journal of the American Chemical Society*, 132:12170–12171, 9 2010.

[81] Shaojun Guo and Erkang Wang. Synthesis and electrochemical applications of gold nanoparticles. *Analytica Chimica Acta*, 598:181–192, 8 2007.

[82] Corinna Stumm, Sebastian Grau, Florian D. Speck, Felix Hilpert, Valentín Briega-Martos, Karl Mayrhofer, Serhiy Cherevko, Olaf Brummel, and Jörg Libuda. Reduction of oxide layers on au(111): The interplay between reduction rate, dissolution, and restructuring. *Journal of Physical Chemistry C*, 125:22698–22704, 10 2021.

[83] Akansha Goyal, Giulia Marcandalli, Vladislav A. Mints, and Marc T. M. Koper. Competition between co2 reduction and hydrogen evolution on a gold electrode under well-defined mass transport conditions. *Journal of the American Chemical Society*, 142(9):4154–4161, 2020. PMID: 32041410.

[84] M. Baldauf and D. M. Kolb. Formic acid oxidation on ultrathin pd films on au(hkl) and pt(hkl) electrodes. *Journal of Physical Chemistry*, 100:11375–11381, 7 1996.

[85] Tamás Pajkossy, Thomas Wandlowski, and Dieter M. Kolb. Impedance aspects of anion adsorption on gold single crystal electrodes. *Journal of Electroanalytical Chemistry*, 414:209–220, 1 1996.

[86] O. M. Magnussen, J. Wiechers, and R. J. Behm. In situ scanning tunneling microscopy observations of the potential-dependent (1 × 2) reconstruction on au(110) in acidic electrolytes. *Surface Science*, 289:139–151, 5 1993.

[87] Serhiy Cherevko, Angel A. Topalov, Ioannis Katsounaros, and Karl J.J. Mayrhofer. Electrochemical dissolution of gold in acidic medium. *Electrochemistry Communications*, 28:44–46, 3 2013.

[88] Corinna Stumm, Manon Bertram, Maximilian Kastenmeier, Florian D Speck, Zhaozong Sun, Jonathan Rodríguez-Fernández, Jeppe V Lauritsen, Karl J J Mayrhofer, Serhiy Cherevko, Olaf Brummel, Jörg Libuda, C Stumm, M Bertram, M Kastenmeier, O Brummel, J Libuda, F D Speck, K J J Mayrhofer, S Cherevko, Z Sun, J Rodríguez-Fernández, and J V Lauritsen. Structural dynamics of ultrathin cobalt oxide nanoislands under potential control. *Advanced Functional Materials*, 31:2009923, 3 2021.

[89] Marie Anne Schneeweiss, Dieter M. Kolb, Dezhong Liu, and Daniel Mandler. Anodic oxidation of au(111). *Canadian Journal of Chemistry*, 75(11):1703–1709, 1997.

[90] Stanley Bruckenstein and Michael Shay. An in situ weighing study of the mechanism for the formation of the adsorbed oxygen monolayer at a gold electrode. *Journal of Electroanalytical Chemistry and Interfacial Electrochemistry*, 188:131–136, 6 1985.

[91] Shen Ye, Chikara Ishibashi, Katsuaki Shimazu, and Kohei Uosaki. An in situ electrochemical quartz crystal microbalance study of the dissolution process of a gold electrode in perchloric acid solution containing chloride ion. *Journal of The Electrochemical Society*, 145:1614–1623, 5 1998.

[92] S. Manne, J. Massie, V. B. Elings, P. K. Hansma, and A. A. Gewirth. Electrochemistry on a gold surface observed with the atomic force microscope. *Journal of Vacuum Science and Technology B: Microelectronics and Nanometer Structures Processing, Measurement, and Phenomena*, 9:950–954, 3 1991.

[93] Carissima M. Vitus and Alison J. Davenport. In situ scanning tunneling microscopy studies of the formation and reduction of a gold oxide monolayer on au(111). *Journal of The Electrochemical Society*, 141(5):1291, may 1994.

[94] Xiaoping Gao and Michael J. Weaver. Nanoscale structural changes upon electro-oxidation of au(111) as probed by potentiodynamic scanning tunneling microscopy. *Journal of Electroanalytical Chemistry*, 367(1):259–264, 1994.

[95] Dennis J. Trevor and Christopher E. D. Chidsey. Room temperature surface diffusion mechanisms observed by scanning tunneling microscopy. *Journal of Vacuum Science and Technology B: Microelectronics and Nanometer Structures Processing, Measurement, and Phenomena*, 9:964–968, 3 1991.

[96] Shen Ye, Chikara Ishibashi, and Kohei Uosaki. Anisotropic dissolution of an au(111) electrode in perchloric acid solution containing chloride anion investigated by in situ stmthe important role of adsorbed chloride anion. *Langmuir*, 15:807–812, 2 1998.

[97] Hidetoshi Honbo, Shizuowara Suga, and Kingo Itaya. Detailed in situ scanning tunneling microscopy of single crystal planes of gold(111) in aqueous solutions. *Analytical Chemistry*, 62:2424–2429, 11 1990.

[98] M. Kleinert, A. Cuesta, L.A. Kibler, and D.M. Kolb. In-situ observation of an ordered sulfate adlayer on au(100) electrodes. *Surface Science*, 430(1):L521–L526, 1999.

[99] Angel Cuesta, Markus Kleinert, and Dieter M. Kolb. The adsorption of sulfate and phosphate on au(111) and au(100) electrodes: an in situ stm study. *Phys. Chem. Chem. Phys.*, 2:5684–5690, 2000.

[100] O. M. Magnussen, B. M. Ocko, R. R. Adzic, and J. X. Wang. X-ray diffraction studies of ordered chloride and bromide monolayers at the au(111)-solution interface. *Physical Review B*, 51:5510, 2 1995.

[101] A. Cuesta and D.M. Kolb. The structure of bromide and chloride adlayers on au(100) electrodes: an in situ stm study. *Surface Science*, 465(3):310–316, 2000.

[102] Ariba Adnan, Saeid Behjati, Núria Félez-Guerrero, Kasinath Ojha, and Marc T. M. Koper. Tracking the surface structure and the influence of cations and anions on the double-layer region of a au(111) electrode. *Phys. Chem. Chem. Phys.*, 26:21419–21428, 2024.

[103] A. Hamelin and S. Röttgermann. Cyclic voltammograms of the au(100) face. *Electrochimica Acta*, 32:723–724, 4 1987.

[104] S. Štrbac, R. R. Adžć, and A. Hamelin. Oxide formation on gold single crystal stepped surfaces. *Journal of Electroanalytical Chemistry and Interfacial Electrochemistry*, 249:291–310, 7 1988.

[105] H. Angerstein-Kozlowska, B. E. Conway, A. Hamelin, and L. Stoicoviciu. Elementary steps of electrochemical oxidation of single-crystal planes of au—i. chemical basis of processes involving geometry of anions and the electrode surfaces. *Electrochimica Acta*, 31:1051–1061, 8 1986.

[106] H. Angerstein-Kozlowska, B. E. Conway, A. Hamelin, and L. Stoicoviciu. Elementary steps of electrochemical oxidation of single-crystal planes of au part ii. a chemical and structural basis of oxidation of the (111) plane. *Journal of Electroanalytical Chemistry and Interfacial Electrochemistry*, 228:429–453, 8 1987.

[107] H. Angerstein-Kozlowska, B. E. Conway, K. Tellefsen, and B. Barnett. Stochastically-gated surface processes involving anions in oxidation of au: time-resolution of processes down to 0.25% coverages and 50 μs time-scales. *Electrochimica Acta*, 34:1045–1056, 8 1989.

[108] Holly Walen, Da-Jiang Liu, Junepyo Oh, Hyunseob Lim, J. W. Evans, Yousoo Kim, and P. A. Thiel. Self-organization of s adatoms on au(111): $\sqrt{3}$r30° rows at low coverage. *The Journal of Chemical Physics*, 143(1):014704, 07 2015.

[109] Saeid Behjati and Marc T. M. Koper. Effect of trace amounts of chloride on roughening of au(111) single-crystal electrode surface in sulfuric acid solution during oxidation–reduction cycles. *ACS Electrochemistry*, 1(7):1082–1092, 2025.

[110] V. Maurice, H.-H. Strehblow, and P. Marcus. In situ stm study of the initial stages of oxidation of cu(111) in aqueous solution. *Surface Science*, 458(1):185–194, 2000.

[111] M. Wilms, M. Kruft, G. Bermes, and K. Wandelt. A new and sophisticated electrochemical scanning tunneling microscope design for the investigation of potentiodynamic processes. *Review of Scientific Instruments*, 70(9):3641–3650, 09 1999.

[112] Klaus Wandelt Knud Gentz. Electrochemical scanning tunneling microscopy. *CHIMIA*, 66(1/2):44, Feb. 2012.

[113] Richard Sonnenfeld and Paul K. Hansma. Atomic-resolution microscopy in water. *Science*, 232(4747):211–213, 1986.

[114] Dong-Yuan Sheng and Qiang Yue. Modeling of fluid flow and residence-time distribution in a five-strand tundish. *Metals*, 10(8), 2020.

[115] Robert E. Treybal. *Mass-Transfer Operations*. McGraw-Hill Book Company, New York, 3rd edition, 1980.

[116] Flow Science, Inc. *Flow-3D User Manual: v10.1*. Flow Science, Inc., Santa Fe, NM, 2012.

[117] C.W Hirt and B.D Nichols. Volume of fluid (vof) method for the dynamics of free boundaries. *Journal of Computational Physics*, 39(1):201–225, 1981.

[118] Francis H. Harlow and J. Eddie Welch. Numerical calculation of time-dependent viscous incompressible flow of fluid with free surface. *The Physics of Fluids*, 8(12):2182–2189, 12 1965.

[119] Octave Levenspiel. *Chemical Reaction Engineering*. Wiley, New York, 3rd edition, 1998.

[120] Tingyi "Leo" Liu and Chang-Jin "CJ" Kim. Contact angle measurement of small capillary length liquid in super-repelled state. *Scientific Reports*, 7(1):740, 2017.

[121] P.V. Danckwerts. Continuous flow systems. distribution of residence times. *Chemical Engineering Science*, 2(1), 1958.

[122] Shaofan Li and Gang Wang. Introduction of Dislocation Theory. In *Introduction to Micromechanics and Nanomechanics*, pages 341–411. WORLD SCIENTIFIC, feb 2018.

[123] Serhiy Cherevko, Angel A. Topalov, Aleksandar R. Zeradjanin, Ioannis Katsounaros, and Karl J. J. Mayrhofer. Gold dissolution: towards understanding of noble metal corrosion. *RSC Advances*, 3(37):16516, 2013.

[124] S. H. Cadle and Stanley Bruckenstein. Ring-disk electrode study of the anodic behavior of gold in 0.2m Sulfuric acid. *Analytical Chemistry*, 46(1):16–20, 1974.

[125] S. Vesztergom, M. Ujvári, and G.G. Láng. RRDE experiments with potential scans at the ring and disk electrodes. *Electrochemistry Communications*, 13(4):378–381, apr 2011.

[126] Buddha Ratna Shrestha, Atsushi Nishikata, and Tooru Tsuru. Application of channel flow double electrode to the study on gold dissolution during potential cycling in sulfuric acid solution. *Journal of Electroanalytical Chemistry*, 665:33–37, jan 2012.